How are Vorticity Rivers in Supercell Storms Produced and Are They Important Vorticity Sources for Tornadoes?

Wei Huang[a] and Ming Xue[b]

[a] *Key Laboratory of Mesoscale Severe Weather/Ministry of Education, School of Atmospheric Sciences, Nanjing University, Nanjing, Jiangsu 210023, China*

[b] *Center for Analysis and Prediction of Storms and School of Meteorology, University of Oklahoma, Norman, OK 73072, USA*

Submitted to J. Atmospheric Science

October 13, 2024

Revised March 19, 2025, June 13, 2025

Corresponding author

Ming Xue, mxue@ou.edu

Early Online Release: This preliminary version has been accepted for publication in *Journal of the Atmospheric Sciences*, may be fully cited, and has been assigned DOI 10.1175/JAS-D-24-0227.1. The final typeset copyedited article will replace the EOR at the above DOI when it is published.

ABSTRACT

A vorticity river is defined as a near-ground vertical vorticity band often extending from the north side of a supercell towards an incipient or mature tornado. Three successive vorticity rivers in a numerical simulation of a supercell tornado are found after the tornado has fully formed. Air parcels that enter the vorticity rivers first ascend in the inflow region of the supercell south of the forward-flank convergence boundary (FFCB) while moving northwestward. Upon approaching the downdraft region north of the FFCB, the air parcels start to descend and turn westwards then southwards towards the tornadic region, converting the crosswise vorticity that the parcels initially carry into the streamwise vorticity. The horizontal streamwise vorticity of the parcels is enhanced by horizontal stretching when the flow accelerates towards the tornadic region. Near-ground positive vertical vorticity develops via upward tilting of horizontal streamwise vorticity as the air parcels descend along a gradually decreasing slope. As the parcels enter the region of strong surface convergence generated by downdrafts of varying intensity on both sides of the vorticity river, their vertical vorticity is further intensified by upward tilting of horizontal vorticity and vertical stretching. The calculated influxes of horizontal and vertical vorticity into the tornadic region show that the contribution to the tornado vorticity by the vorticity rivers is minimal given their narrow width and shallow depth. Backward trajectory analysis shows that only about 7% of total parcels entering the tornado originate from vorticity rivers, suggesting that their direct contribution to tornado intensification or maintenance is insignificant.

SIGNIFICANCE STATEMENT

A vorticity river is a narrow band of vertical vorticity extending from the north side of simulated supercell storms southward towards an intensifying or mature tornado. The source of vorticity in the vorticity river and its contribution to tornado formation and maintenance are examined based on a tornado simulation. Trajectory analyses show that the vertical vorticity in vorticity rivers is generated first by upward tilting of horizontal vorticity and then intensified rapidly by near-ground vertical stretching due to along-river convergence. Budget calculations of vorticity into the tornadic region show that the contribution of the narrow and shallow vorticity rivers to the intensification and maintenance of tornado is limited. Only a very small fraction of air parcels entering the tornado pass through the rivers. The primary source of both vertical

Accepted for publication in *Journal of the Atmospheric Sciences*. DOI 10.1175/JAS-D-24-0227.1.

and horizontal vorticity inflow into the tornadic region comes from the occlusion zone on the northeast side of the tornado.

Accepted for publication in *Journal of the Atmospheric Sciences.* DOI 10.1175/JAS-D-24-0227.1.

1. Introduction

During the incipient and mature stages of tornadoes, bands of enhanced vertical vorticity near the ground feeding into the tornado vortex have been noted in numerical simulations of supercells. These bands are often situated to the north or northwest of the tornado vortex (Beck and Weiss 2013; Oliveira et al. 2019; Boyer and Dahl 2020; Fischer and Dahl 2020). Dahl et al. (2014) noticed such vertical vorticity bands in their idealized supercell simulation at 250 m grid spacing and called the bands "vorticity rivers". A similar feature is present in the schematic of tornadoes in Fujita et al. (1976) and Fujita called the band "vorticity feeder". The vorticity rivers have been suggested to possibly provide an important vorticity source that feeds into a developing or a mature tornado (Dahl et al. 2014).

A vorticity river is often in a similar orientation as the left-flank convergence boundary (LFCB) defined by Beck and Weiss (2013) based on a simulation of a mature supercell (at 250 m horizontal grid spacing), and both are located on the north side of any incipient or mature tornado or mesocyclone. The LFCB is a convergence boundary with a significant equivalent potential temperature gradient across the boundary. The air west of the boundary is colder due to evaporative cooling, and the density differences are believed to be responsible for the convergence along the boundary, even though the winds are generally northerly on both sides (Beck and Weiss 2013). In the supercell simulation (at 50 m grid spacing) by Markowski et al. (2014), they also noted the existence of a northward extending boundary with positive vertical vorticity, which separates rear-flank outflow from forward-flank outflow, and the boundary is suggested to be the same LFCB identified in Beck and Weiss (2013). Markowski et al. (2014) focused, however, on the analysis of two other vorticity bands or vortex sheets, one along the forward-flank convergence boundary (FFCB) and one along the rear-flank gust front (RFGF).

Multiple alternating vortex rivers are also identified in the idealized simulations of a downdraft forced by an idealized heat sink in Parker and Dahl (2015). Utilizing composite near-storm environments of nontornadic and tornadic supercells observed during the second Verification of the Origins of Rotation in Tornadoes Experiment (VORTEX2), Coffer and Parker (2017) and Coffer et al. (2017) simulated tornadic and nontornadic supercells, and found the existence of vorticity rivers in both nontornadic

Accepted for publication in *Journal of the Atmospheric Sciences*. DOI 10.1175/JAS-D-24-0227.1.

and tornadic cases. In the tornadic supercells, the vorticity river exhibits a north-south stationary orientation during peak intensity, while the orientation is not stationary in nontornadic supercells. The existence of vorticity rivers is also noted in other idealized tornadic storm simulations (Oliveira et al. 2019; Sherburn and Parker 2019). Vorticity rivers are also evident in some members of a tornado-resolving forecast ensemble of an observed tornado event initialized using ensemble Kalman filter data assimilation (Snook et al. 2019).

Although vorticity rivers are present in many of the simulations mentioned above, few studies have delved into analyzing the formation mechanism of the vorticity rivers. Based on trajectory analysis of an idealized simulation of a supercell storm (at 250 m grid spacing) with free slip lower boundary condition, Dahl et al. (2014) proposed that the downdraft mechanism of Davies-Jones and Brooks (1993) or the DJB mechanism is responsible for the generation of vertical vorticity in vorticity rivers in their simulation. The DJB mechanism was originally proposed to explain the development of vertical vorticity needed for near-ground tornado vortex intensification. With the mechanism, horizontal vorticity generated baroclinically when a parcel descends towards the ground near the periphery of a downdraft is partially tilted into the vertical direction before the parcel reaches its nadir (the lowest point) along its trajectory when the slope of the trajectory decreases while descending. The vertical vorticity is then amplified dramatically by stretching, leading to tornadogenesis. In the case of the vorticity river, the process produces the vertical vorticity along the river in Dahl et al. (2014). When analyzing the vortex sheets along the FFCB and RFGF, Markowski et al. (2014) also emphasize the importance of baroclinically generated horizontal vorticity associated with cold low-level outflow and the necessity of a sinking motion for the generation of the vortex sheets. Dahl et al. (2014) and Markowski et al. (2014) are two existing studies that examined, to some degree, the source of vorticity in the vorticity river or similar structures. Both of their simulations used a free-slip lower boundary condition; therefore, no vorticity can be generated by surface drag. More recent studies have shown that significant horizontal vorticity can also be generated by surface drag, when it is included in the model via a semi-slip lower boundary condition (Schenkman et al. 2014; Xu et al. 2015; Markowski 2016; Roberts et al. 2016; Roberts and Xue 2017; Yokota et al. 2018; Tao and Tamura 2020). Recently, Jiang and Dawson (2023) studied the impact of surface drag introduced into a supercell simulation a few minutes

Accepted for publication in *Journal of the Atmospheric Sciences*. DOI 10.1175/JAS-D-24-0227.1.

prior to tornadogenesis, on the structure and evolution of surface boundaries. A much more pronounced LFCB develops in the simulation with surface drag. Substantial drag-generated horizontal vorticity induces rotor structures along the convergence boundary. On the ascending branch of the rotor, the stretching of horizontal vorticity and subsequent tilting into the vertical along the convergence boundary lead to an elongated positive vertical vorticity sheet on the ascending branch of the rotor and the opposite on the descending branch, which aids in the enhanced generation of surface vertical vorticity. Because the storm-scale surface drag was not introduced into the simulation until 10 minutes prior to tornadogenesis in Jiang and Dawson (2023), there are uncertainties with the formation mechanisms of the LFCB and associated vorticity structure discussed in their paper.

The role of vorticity rivers in the development and maintenance of tornadoes remains unclear, and existing studies offer divergent views. The vorticity rivers are seen to move downstream and appear to be fed into the developing vortex (Dahl et al. 2014), suggesting that vorticity advected into a tornado vortex may facilitate tornadogenesis. The 250 m horizontal grid spacing of Dahl et al. (2014) is not high enough to simulate tornadogenesis, however. Oliveira et al. (2019) also suggest that the vorticity river is a possible source of vertical vorticity for low-level rotation in their tornadic supercell simulation at 100 m grid spacing. Boyer and Dahl (2020) simulated several storm modes at 200 m grid spacing and suggested that the presence of vorticity rivers is not necessary for tornadogenesis. In their supercell simulation, parcels do not pass through vorticity rivers, and vorticity rivers are even absent in their squall-line simulation. Therefore, existing studies either raise questions or provide only qualitative assessments of the contribution of vorticity rivers to tornadogenesis, tornado intensification, or maintenance; there is a general lack of quantitative analysis of its contribution so far.

There are two possible ways that vorticity rivers facilitate tornadogenesis or tornado maintenance. On one hand, vorticity rivers can facilitate tornadogenesis or maintenance by directly feeding vertical vorticity to the tornado region, which is subsequently stretched and intensified. This potential role was suggested by Dahl et al. (2014). If pre-tornadic vertical vorticity near the ground is necessary for tornadogenesis (e.g., Davies-Jones and Brooks 1993), then the positive vorticity carried by the river can indeed be

Accepted for publication in *Journal of the Atmospheric Sciences*. DOI 10.1175/JAS-D-24-0227.1.

very important. Vorticity rivers can also contain substantial horizontal streamwise vorticity (Parker and Dahl 2015; Coffer and Parker 2017) that is fed into the tornado region and tilted into the vertical abruptly to cause tornadogenesis (Rotunno et al. 2017) or through the in-and-up mechanism to support established tornadoes (Boyer and Dahl 2020; Fischer and Dahl 2022; Fischer et al. 2024). It is also possible that vorticity rivers do not play a significant role in tornadogenesis, or tornado maintenance.

The existence of vorticity rivers is also noted in the simulation of a real EF4 tornado that occurred in Funing, China, in Sun et al. (2019). High-frequency simulation outputs are produced and available for detailed, quantitative analyses on the origin of the vorticity rivers and their contribution to tornado development in different stages. In this study, we aim to address the following questions, specifically focused on vorticity rivers in the simulated Funing tornado: What is the formation mechanism of the vorticity rivers? Do vorticity rivers play an important role in tornado development in different stages, and what are the relative contributions of vorticity rivers to tornado development in terms of the vertical vorticity and horizontal vorticity supply? Based on the analyses, the most important influxes of vorticity into the tornadic region are also suggested.

The remainder of the paper is organized as follows: Section 2 provides a case overview of the Funing tornado case and presents the simulated results for examination. Section 3 analyzes the formation mechanisms of vorticity rivers in terms of vorticity source. Section 4 calculates the quantitative contributions of vorticity rivers to tornado development in terms of vorticity influx and performs trajectory analyses to determine how many parcels entering the tornado originate from the vorticity river. A summary and conclusions are given in Section 5.

2. Numerical simulation of Funing tornado

The tornado of interest occurred in Funing Country, Yancheng City, in northern Jiangsu Province, in the afternoon of June 23, 2016. Field damage surveys suggested an EF4 intensity (Xue et al. 2016). Under the influence of a quasi-stationary cold vortex in northeastern China at 500 hPa, an 850 hPa trough, and the western Pacific sub-tropical high, the environment was particularly unstable, with maximum unstable

Accepted for publication in *Journal of the Atmospheric Sciences*. DOI 10.1175/JAS-D-24-0227.1.

convective available potential energy (CAPE) being 2663 J kg^{-1} and convective inhibition (CIN) being 8 J kg^{-1}, which was very conducive to the occurrence of strong convection. The Funing tornado was spawned by a supercell storm that developed south of a Meiyu frontal rainband. The hook echo, wrapped with the tornado, was most pronounced from 0603 to 0631 UTC and mostly vanished at about 0700 UTC. The tornado reached EF4 intensity at about 0620 UTC and again at 0635 UTC, and the actual tornado lasted from 0615 to 0700 UTC. The specific atmospheric conditions under which the Funing tornado occurred have been described by Xue et al. (2016), Meng et al. (2018), and Sun et al. (2019).

Sun et al. (2019) simulated the Funing tornado using the advanced research version of the Weather Research and Forecasting (WRF-ARW) model with five levels of nested grids. The simulated tornado on the highest-resolution grid reaches EF3 intensity based on surface wind speed. The formation mechanism of the multiple 'suction vortices' in the simulation is studied by Huang and Xue (2023) as caused by the nonlinear intensification of vortex Rossby waves due to barotropic instability along a vorticity ring.

The simulation of Sun et al. (2019) is rerun to produce output at 1-second intervals. In Sun et al. (2019), the exact time of tornadogenesis was clearly defined. They simply referred to the presence of a strong near-surface vortex as a tornado (e.g., at 0655 UTC). Previous studies often use the maximum wind speed and vertical vorticity exceeding certain threshold values as the criteria. However, given that the pre-tornadic vortex was initially weaker than some of the small vortices that were eventually absorbed into the pre-tornadic vortex (see their Fig. 9), it was not straightforward to use specific wind speed and vertical vorticity thresholds to define the tornadogenesis time, at least in their study. In our study, we define tornadogenesis as the time when maximum vertical vorticity is found at the ground (the lowest model level above ground) in the main vortex, V0, and when the strong vertical vorticity becomes continuously aligned from the ground upward. Such criteria are consistent with high-resolution radar observational studies, including those of French et al. (2013), Houser et al. (2015), and Bluestein et al. (2019). In their observations, the tornado vortex signature (TVS) is initially weaker at low levels above the surface compared to lower or higher altitudes, just prior to and during the early stages of tornadogenesis. The tornadogenesis is successful when the

Accepted for publication in *Journal of the Atmospheric Sciences*. DOI 10.1175/JAS-D-24-0227.1.

low-level mesocyclone intensifies to align with strong rotation near the surface, forming a coherent tornado column. According to our criteria given above, and based on three-dimensionally rendered vertical vorticity fields (figure not shown), the time of tornadogenesis for the main vortex, V0, is identified as 0703:20 UTC. The tornado was fully established at ~0707 UTC with a well-formed vortex. After 0707 UTC, the intensity of the tornado increases and reaches its maximum surface vertical vorticity around 0724 UTC in the simulation (figure not shown). The timing and location of the simulated tornado are somewhat different from the observations. In observations, it reached EF4 intensity at 0630 UTC. The Funing tornado in the simulation is displaced northward compared to the observed position (refer to Fig. 15 in Meng et al. 2018 and Fig. 11 in Sun et al. 2019). Since our emphasis is on the generation mechanism of vorticity rivers, inaccuracies in the timing and location are less important.

Two main boundaries within the low-level wind field can be observed in our simulation (Fig. 1). One boundary that extends south from the tornado vortex is the RFGF. Across the RFGF, strong gradients of perturbation density potential temperature (θ_ρ'; Emanuel 1994, p. 161) and decreasing strength of convergence from west to east are observed. Another boundary separating the southeasterly from the northeasterly winds extends eastward from the tornado vortex. The θ_ρ' gradient is weak across this boundary. It is the FFCB as defined in Beck and Weiss (2013).

As described in more detail in Sun et al. (2019), the innermost domain measures 117 km × 94 km and has a horizontal grid spacing of 49 m. The vertical grid is stretched with the lowest model level above ground being at 10 m. Surface drag has been shown to be important for tornadogenesis according to recent studies (e.g., Schenkman et al. 2014; Xu et al. 2015; Schenkman et al. 2016; Roberts et al. 2016; Roberts and Xue 2017; Yokota et al. 2018; Tao and Tamura 2020). In the simulation, surface drag, in terms of the surface momentum fluxes, is calculated by the surface physics scheme based on local surface roughness conditions (the tornadic region is mostly flat farmland) and stability. The roughness length in the region of the tornado storm is about 0.1–0.8 m. A fully three-dimensional 1.5-order turbulent kinetic energy (TKE)-based subgrid-scale (SGS) turbulence closure scheme based on Deardorff (1974) is used only on the innermost domain, while Smagorinsky deformation-based horizontal SGS turbulence mixing parameterization (Smagorinsky 1963) is used on the other grids. The Pleim-Xiu

Accepted for publication in *Journal of the Atmospheric Sciences*. DOI 10.1175/JAS-D-24-0227.1.

land surface and surface layer models (Pleim 2006) coupled with the Asymmetric Convective Model (Version 2, ACM2) PBL scheme (Pleim 2007) are used on all grids. All five grids use the 2-moment Morrison microphysics scheme (Morrison and Grabowski 2008).

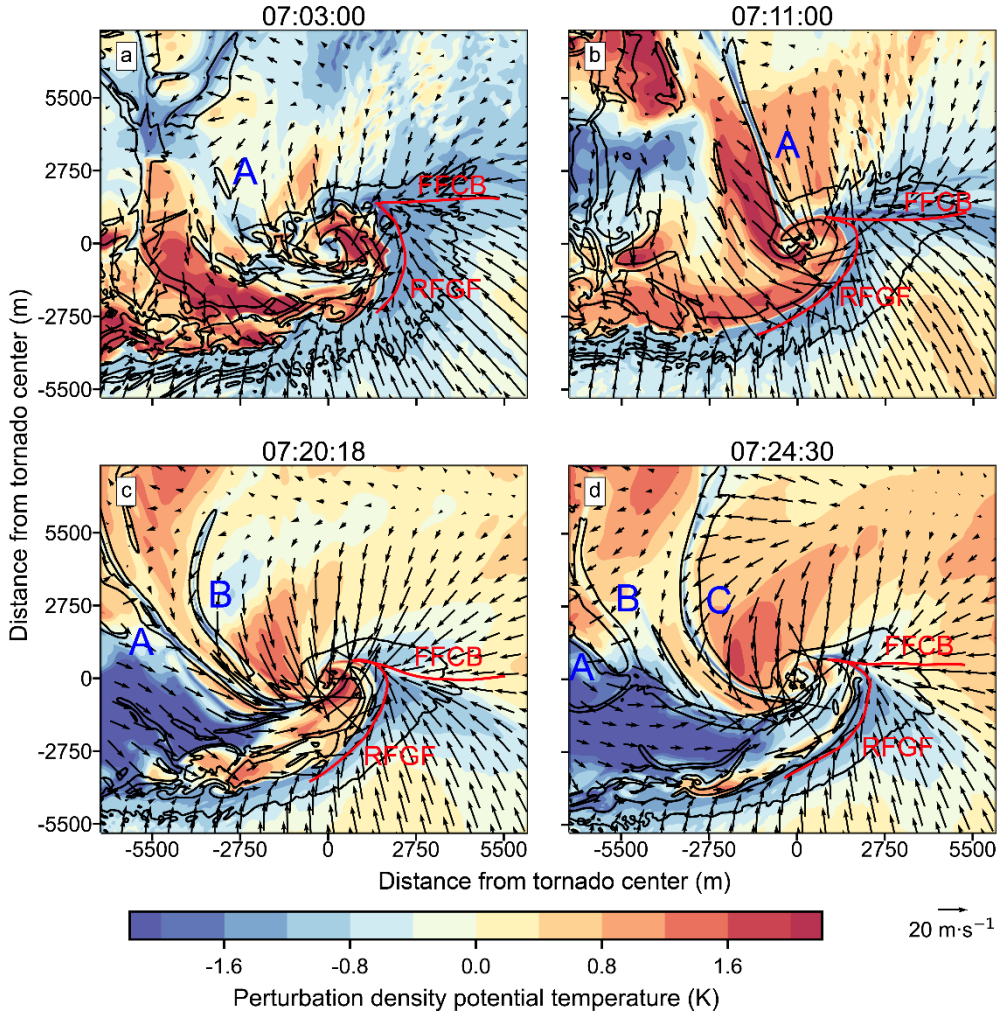

Fig. 1. Perturbation density potential temperature, θ'_ρ (K; shaded) and convergence values (black contours at 0.02 s^{-1}) at (a) 0703:00, (b) 0711:00, (c) 0720:18, and (d) 0724:30 UTC with ground-relative wind vectors at 26 m. The *x* and *y* axes shift with the tornado vortex and are in meters. FFCB and RFGF are denoted by red lines and are drawn mainly based on the flow pattern. Three vorticity rivers labeled A, B, and C, which match the locations of convergence bands, will be discussed in Section 3.

3. The formation mechanism of vorticity rivers

a. The evolution of three vorticity rivers in the simulation

Accepted for publication in *Journal of the Atmospheric Sciences*. DOI 10.1175/JAS-D-24-0227.1.

In this study, a vorticity river is defined as a positive ζ band with a value greater than 0.004 s^{-1} that extends outward from the tornado vortex (which can be a vortex that later develops into a tornado) mostly towards the north side and exists for more than two minutes. According to this criterion, we found three vorticity bands satisfying the conditions (Fig. 2, labeled vorticity rivers A, B, and C). These three vorticity rivers are all located between the RFGF and FFCB (Fig. 1b–d). The vorticity rivers can be seen after 0709:30 UTC, which is after tornadogenesis (Fig. 2d). Vorticity river A first appears at about 0709:30 UTC (Fig. 2d), then strengthens and matures by 0711 UTC (Fig. 2e) with a strong convergence (Fig. 1b). At the mature stage, the vorticity band becomes continuous and ζ exceeds 0.008 s^{-1}. Vorticity river A subsequently rotates cyclonically to the northwest and then the west side of the tornado (Fig. 2e–g). A hint of vorticity river B first appears at 0718:48 UTC (Fig. 2h) and becomes fully developed by 0720:18 UTC (Fig. 2i) also with a strong convergence (Fig. 1c). It is stronger at its middle and northern sections, although its weaker southern portion does extend to the tornadic region. Pushed by the flows on the east side (Fig. 1c), the southern and middle sections of vorticity river B have caught up with vorticity river A by 0722:12 UTC, merging to become a single band at the inside portion (Fig. 2j). By 0722:45 UTC, the merged section extends outward further while the section closest to the tornado vortex also merges with a vertical vorticity band further ahead. At this time, vorticity river C starts to emerge (Fig. 2k) and reaches maturity by 0724:30 UTC (Fig. 2l). Pushed by near-surface northeasterly flows (Fig. 2d), it also rotates counterclockwise around the tornado vortex like the earlier two vorticity rivers. By this time, vorticity rivers A and B are mostly merged within the plotting domain, and the merged river has become discontinuous.

Clearly, the three vorticity rivers share many common characteristics. They all form initially on the north or northwest side of the tornado vortex, then extend southward and connect with the tornado vortex as they mature. Pushed by the cyclonic circulation around the intensifying/mature tornado, especially by the strong northeasterly winds from north of FFCB, the vorticity rivers rotate counterclockwise towards the west side of the tornado and gradually stall on the southwest behind the RFGF. The rivers eventually merge together and dissipate. The initiation position and morphological characteristics are similar to the vorticity rivers described by Dahl et al. (2014),

Accepted for publication in *Journal of the Atmospheric Sciences*. DOI 10.1175/JAS-D-24-0227.1.

although their simulation used a much larger grid spacing (250 m) and therefore, their simulated rivers were wider and much more diffused.

The vorticity rivers in our simulation are mostly dominated by positive vertical vorticity, but they are also sometimes accompanied by a weaker band of negative vertical vorticity. In the simulations of Dahl et al. (2014) and Jiang and Dawson (2023), weak negative vorticity bands also exist on the east side of the rivers. Sherburn and Parker (2019) also found alternating positive and negative ζ bands emanating from the convective downdraft in the idealized simulation of strong surface vortices developing within high-shear and low-CAPE environments. In the real case simulations of Snook et al. (2019), streamer-like regions of enhanced updraft are found, which are akin to the "vorticity river" features and are accompanied by negative vertical vorticity in at least one member of their ensemble simulations. Also worth noting is that none of the three vorticity rivers in our simulation is in a quasi-steady position relative to the tornado vortex, as in Dahl et al. (2014) (relative to the rotation center in their case). Nonstationary vorticity rivers are also seen in the simulations of Coffer and Parker (2017).

Accepted for publication in *Journal of the Atmospheric Sciences.* DOI 10.1175/JAS-D-24-0227.1.

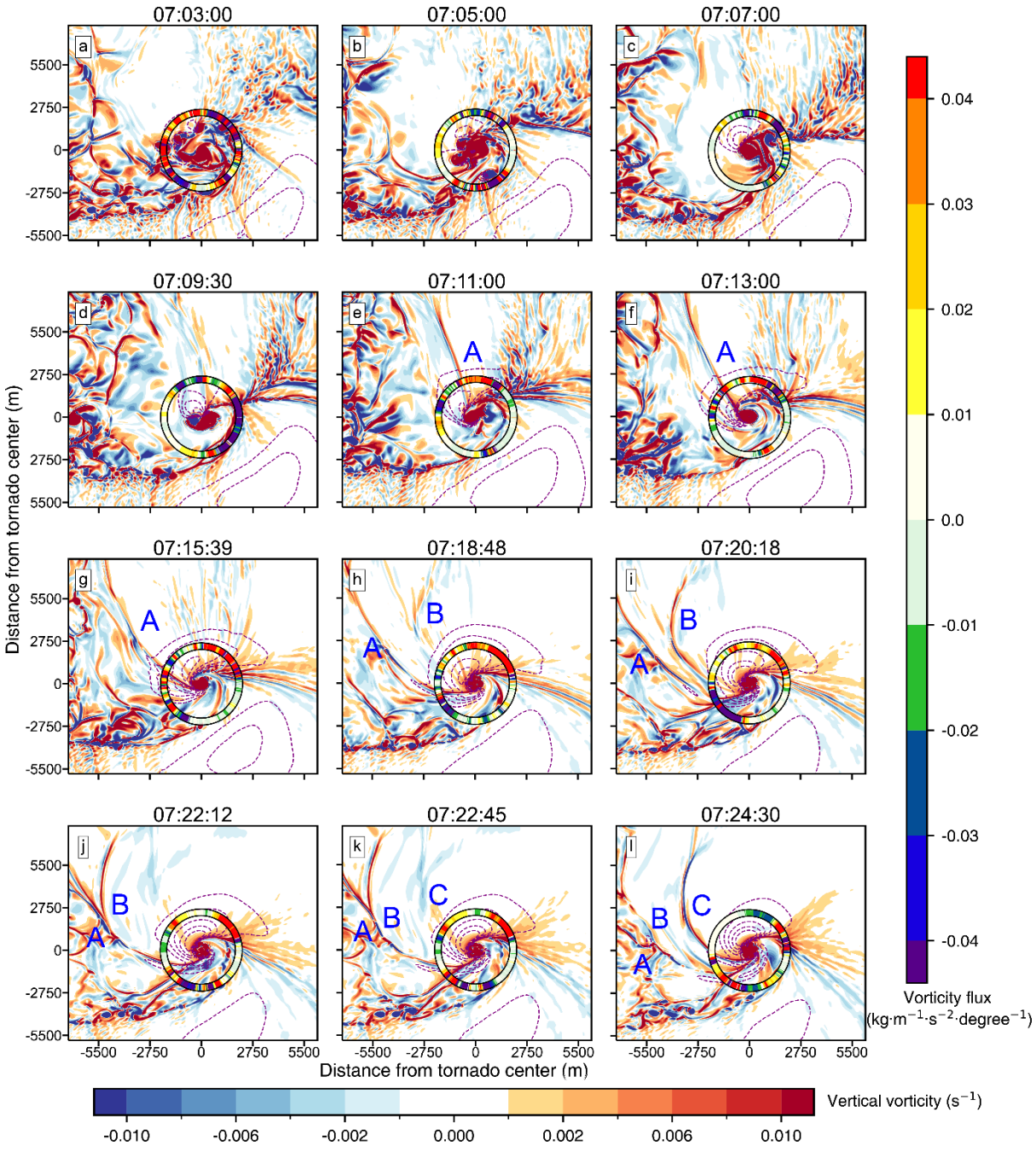

Fig. 2. Vertical vorticity (ζ, s^{-1}) at (a) 0703:00, (b) 0705:00, (c) 0707:00, (d) 0709:30, (e) 0711:00, (f) 0713:00, (g) 0715:39, (h) 0718:48, (i) 0720:18, (j) 0722:12, (k) 0722:45, and (l) 0724:30 UTC overlaid with radial wind (dashed contours at 20, 25, 30, 35, 40 m s^{-1}) and a circle with black edges around the tornado vortex that is colored by the radial influx of vertical vorticity (kg m^{-1} s^{-2} $degree^{-1}$) at 26 m AGL. The *x* and *y* axes shift with the tornado vortex and are in meters. Three vorticity rivers are labeled A, B, and C. The flux ring is 1-m tall for calculation purposes.

In our simulation, tornadogenesis first occurs at 0703:20 UTC, while the vorticity rivers are not observed until after 0709:30 UTC. Based on the timing, the vorticity

Accepted for publication in *Journal of the Atmospheric Sciences*. DOI 10.1175/JAS-D-24-0227.1.

rivers are unlikely to have directly contributed vertical vorticity to the vortex intensification processes that lead to tornadogenesis. If anything, they can only contribute to the intensification and maintenance of the tornado in our case. The contributions of vorticity rivers to the intensification and maintenance of the tornado will be quantitatively analyzed in Section 4.

b. Trajectory-based vorticity budgets for three vorticity rivers

To determine the main source of near-ground vertical vorticity in the three vorticity rivers, backward trajectory and Lagrangian integrations of vorticity equations in streamwise, crosswise, and vertical directions are performed for the three vorticity rivers. The horizontal vorticity is decomposed into streamwise (ω_s) and crosswise (ω_n) components in semi-natural coordinates (*s*, *n*, *k*). *s* is along horizontal wind direction and *n* is perpendicular to and point to the left of *s* (Lilly 1982; Adlerman et al. 1999). The vorticity tendency equations are

$$\frac{D\omega_s}{Dt} = \omega_n \frac{D\psi}{Dt} + \boldsymbol{\omega} \cdot \boldsymbol{\nabla V} + \frac{1}{\rho^2}\left(\frac{\partial \rho}{\partial n}\frac{\partial p}{\partial z} - \frac{\partial \rho}{\partial z}\frac{\partial p}{\partial n}\right) + \left(\frac{\partial F_z}{\partial n} - \frac{\partial F_n}{\partial z}\right), \quad (1)$$

$$\frac{D\omega_n}{Dt} = -\omega_s \frac{D\psi}{Dt} + \boldsymbol{\omega} \cdot \boldsymbol{V\nabla}\psi + \frac{1}{\rho^2}\left(\frac{\partial \rho}{\partial z}\frac{\partial p}{\partial s} - \frac{\partial \rho}{\partial s}\frac{\partial p}{\partial z}\right) + \left(\frac{\partial F_s}{\partial z} - \frac{\partial F_z}{\partial s}\right), \quad (2)$$

$$\frac{D\zeta}{Dt} = \zeta\frac{\partial w}{\partial z} + \left(\omega_s \frac{\partial w}{\partial s} + \omega_n \frac{\partial w}{\partial n}\right) + \frac{1}{\rho^2}\left(\frac{\partial \rho}{\partial n}\frac{\partial p}{\partial s} - \frac{\partial \rho}{\partial s}\frac{\partial p}{\partial n}\right) + \left(\frac{\partial F_n}{\partial s} - \frac{\partial F_s}{\partial n}\right), \quad (3)$$

where $\psi = \tan^{-1}(v/u)$ represents the horizontal direction of the air parcel. Variables $\boldsymbol{\omega}(\omega_s, \omega_n, \zeta)$ and $\boldsymbol{V}$ (u, v, w) are the vorticity and velocity vectors, respectively, and ρ and p are air density and pressure. Quantities F_s, F_n, and F_z are the streamwise, crosswise, and vertical components of the frictional force, respectively. The first terms on the right-hand sides of (1) and (2) represent the exchange of vorticity between streamwise and crosswise directions owing to change in parcel direction angle ψ. The other three terms from left to right in (1) and (2) are stretching/tilting of vortex tubes, solenoidal generation, and frictional generation, respectively. The right-hand side of (3), in order, are stretching of vertical vorticity, tilting of horizontal vorticity, solenoidal generation, and frictional generation. Lagrangian-integrated streamwise, crosswise, and

Accepted for publication in *Journal of the Atmospheric Sciences*. DOI 10.1175/JAS-D-24-0227.1.

vertical vorticities along parcel trajectories are compared with Eulerian-integrated vorticities interpolated to the parcel locations for the three vorticity rivers (e.g., the black solid and black dashed lines in Fig. 3). The result is considered dependable if the two versions are in a good agreement for the three vorticity components.

A representative[1] backward trajectory that finally enters vorticity river A at 37 m AGL at 0711 UTC is plotted in Fig. 3a. For all three rivers, the generation processes of vorticities along the trajectories are similar between the representative trajectories and the average trajectories of all parcels entering vorticity rivers. However, the errors between the integrated and interpolated vorticities along the average trajectories are larger than those of the representative trajectories (figures not shown), therefore, we choose to show the budgets of the representative trajectories.

The Lagrangian- and Eulerian-integrated vorticity values along this trajectory are reasonably consistent. Given the complexity of the flows on the high-resolution grid that resolves near-grid-scale turbulence eddy structures, a very good agreement between Lagrangian and Eulerian integrations is generally difficult to achieve (due to their respective numerical integration errors), and more so for vorticity components whose calculations involve additional spatial derivatives.

The parcel possesses significant horizontal streamwise (~0.025 s^{-1}) and crosswise (~0.04 s^{-1}) vorticities at the beginning of the trajectory at 0650 UTC (Fig. 3b and c). The crosswise vorticity is positive and hence leftward pointing. As the parcel moves northwestward from 0650 to 0700 UTC and rises more later on (Fig. 3a), some positive crosswise vorticity ω_c (we use ω_c as an alternative notation for ω_n) is generated by the baroclinic and tilting terms (Fig. 3b). During this period, as the parcel trajectory curves leftward, some of the ω_c is converted into streamwise vorticity ω_s via the river-bend effect (Shapiro 1972; Scorer 1978; Adlerman et al. 1999; Davies-Jones et al. 2001) (Fig. 3c), while the baroclinic process generates a smaller amount of negative ω_s. Between 0700 and 0706 UTC, as the parcel turns leftwards towards southwest more quickly, more of the leftward-pointing ω_c is exchanged into ω_s (Fig. 3b and c). After 0704 UTC, the horizontal stretching of ω_s becomes its main cause of increase, while

[1] Note that the term 'representative' refers to similar generation processes of vorticity components along the trajectory as most parcels that enter the vorticity rivers.

Accepted for publication in *Journal of the Atmospheric Sciences*. DOI 10.1175/JAS-D-24-0227.1.

the tilting term converts ω_s (Fig. 3c) into the vertical direction to cause a rapid increase in ζ (Fig. 3d).

In summary, the ω_s at the beginning of the calculated trajectory segment is ~0.025 s^{-1} and it reaches ~0.07 s^{-1} when the parcel reaches the vorticity river, mostly due to the conversion from ω_c and subsequent stretching. The baroclinically-generated ω_s is negative while the frictional generation (mixing term) is essentially zero (Fig. 3c). Most of the parcel ω_c is present already at the beginning of the calculated trajectory while baroclinic and tilting processes cause a small amount of change in ω_c. The fact that the horizontal vorticity at the beginning of the calculated trajectory is mostly crosswise, with the vector pointing mostly towards the left of the trajectory (Fig. 3a), suggests that the initial horizontal vorticity is most likely generated by surface friction, either as the parcel accelerates towards the storm as inflow, or is generated by surface friction in the environmental sounding (Roberts et al. 2016). The latter is usually referred to as the barotropic vorticity, the vorticity coming from the environment (Dahl et al. 2014). Before the calculated segment, the parcel is located south of the forward-flank convergence boundary (FFCB; Beck and Weiss 2013) in the inflow region where horizontal buoyancy gradient and hence baroclinic vorticity generation should be small (Fig. 3a).

The vertical vorticity ζ is nearly zero at 0650 UTC (Fig. 3d). The parcel descends from ~100 m to ~25 m AGL from 0701 to 0710 UTC, so that tilting causes a decrease in ζ before 0704 UTC. The descending slope of the parcel decreases from about 0705 UTC and reaches its nadir at 0710 UTC (Fig. 3d). The tilting term starts to increase ζ rapidly after 0704 UTC (red line in Fig. 3d) as ω_s is tilted upward into the vertical (blue line in Fig. 3c). This turns ζ from negative to positive by 0708 UTC, before the nadir is reached by the parcel (black dashed line in Fig. 3d). The process of tilting enhanced *horizontal* streamwise vorticity into the vertical during descent is analogous to that in the DJB mechanism, with a key difference that the enhanced horizontal streamwise vorticity is not generated baroclinically as the parcel descends. Instead, the generation of horizontal streamwise vorticity is via the conversion from ω_c, followed by horizontal stretching by southward accelerating air currents during descent (Fig. 3c), which introduces "slippage" between the descending fluid and the vortex lines (Fig. 3d). In short, the increased horizontal ω_s by exchange from ω_c and further enhanced by

Accepted for publication in *Journal of the Atmospheric Sciences*. DOI 10.1175/JAS-D-24-0227.1.

horizontal stretching, is tilted upward as the parcel descends with a decreasing slope. Positive vertical vorticity is created in the process. After the nadir is reached, horizontal convergence along the vorticity river causes the parcel to rise rapidly and the positive vertical vorticity to increase rapidly through vertical stretching (between 0710 and 0711 UTC in Fig. 3d). The trajectory-integrated ζ is intensified from ~0.001 s^{-1} to ~0.01 s^{-1}. In this last minute, the tilting of ω_s is also significant (Fig. 3d). Hence, the positive vertical vorticity along vorticity river A originates mainly from the tilting of horizontal streamwise vorticity.

A single band of positive vertical vorticity will be generated if the horizontal vorticity of parcels entering the near-surface convergence zone is purely streamwise. We note that the parcel also possesses ω_c whose sign may change (Fig. 3d). When the crosswise vorticity tube is tilted by the convergence zone, a negative vertical vorticity band can be created on the left or right side of main vorticity river depending on the sign of ω_c. Within river A, a weaker negative band is found on the west side of the positive band (Fig. 3a). This phenomenon also can be observed with vorticity rivers B and C.

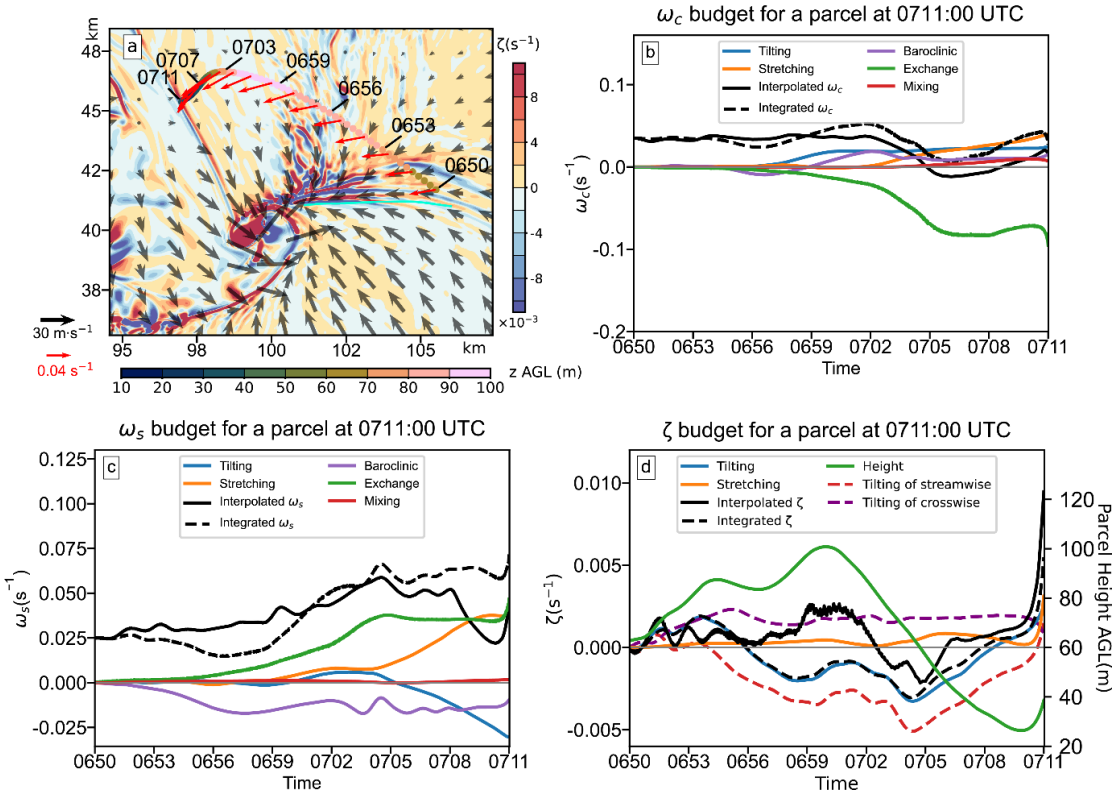

Fig. 3. (a) A representative backward trajectory that terminates at 39 m AGL in vorticity river A at 0711:00 UTC, whose height (m AGL) is shaded in color and

Accepted for publication in *Journal of the Atmospheric Sciences*. DOI 10.1175/JAS-D-24-0227.1.

horizontal vorticity vectors (red arrows, s^{-1}) are plotted at 80 s intervals along the trajectory. Vertical vorticity (shaded, s^{-1}) and ground-relative horizontal wind vectors (black arrows, m s^{-1}) at 38 m AGL at 0711:00 UTC are also shown. Lagrangian vorticity integrations along the trajectory in (a) are plotted for (b) horizontal crosswise vorticity ω_c, (c) horizontal streamwise vorticity ω_s, and (d) vertical vorticity ζ. In (b), the dashed black line is the sum of the time-integrated crosswise stretching (orange line), tilting (blue line), exchange generation (green line), and baroclinic generation (purple line). In (c), the dashed black line is the sum of the time-integrated streamwise stretching (orange line) and tilting (blue line), exchange generation (green line), and baroclinic generation (purple line). In (d), the dashed black line is the sum of the time-integrated vertical stretching (orange line) and tilting (blue line). The tilting is the sum of the tilting of streamwise vorticity (red line) and crosswise vorticity (purple line). The green line in (d) represents the height (m AGL) of the parcel. The solid black line represents the value of crosswise [in (b)], streamwise [in (c)], and vertical [in (d)] vorticity interpolated from the model grid to the parcel location at each time. The locations of the FFCB are marked (cyan line).

Similar trajectory-based analyses are carried out for vorticity river B. The parcel along the representative trajectory of vorticity river B also moves initially northwestwards, then turns westwards, then southwestwards (Fig. 4a) as in the case of river A (Fig. 3a). Before 0712 UTC, ω_s increases while ω_c decreases steadily when ω_c is gradually converted into ω_s. After 0712 UTC, as the parcel starts turning towards the southwest, the conversion accelerates and by 0716 UTC ω_c is all converted into ω_s (Fig. 4a–c). After 0716 UTC, the direction of the parcel changes to almost southward (Fig. 4a), and the parcel joins the convergent airflow into the tornadic region. The associated horizontal stretching in the accelerating flow causes ω_s to rapidly increase (Fig. 4c), and this should continue beyond the calculated trajectory segment. The enhanced stretching, and especially the tilting term, increase ω_c to compensate for the loss caused by the exchange from ω_c to ω_s (Fig. 4b).

The horizontal vorticity generated by baroclinic and frictional processes for river B is minimal before 0716 UTC (Fig. 4b and c). The enhancement from frictionally generated horizontal vorticity does not occur until 0717 UTC, when the parcel gets near the ground. The horizontal vorticity at the beginning of the trajectory is significant.

The ζ of the parcel is negative from the beginning and decreases somewhat after 0711 UTC when the air parcel starts to descend (Fig. 4d). Between 0712 and 0718 UTC, vertical stretching helps to increase ζ. After 0716 UTC, when the parcel descends along

Accepted for publication in *Journal of the Atmospheric Sciences*. DOI 10.1175/JAS-D-24-0227.1.

a decreasing slope (Fig. 4d), the integrated ζ rapidly increases by tilting of the increased ω_s and becomes positive quickly. The stretching term has some negative contribution to ζ to cause it to decrease somewhat between 0718 and 0720 UTC. It then becomes positive again when the parcel reaches its nadir then rapidly rises after 0720 UTC. Afterwards, both tilting of ω_s and the stretching terms contribute to intensifying the positive ζ. For vorticity river B, the dominant term that produces positive ζ is the tilting of enhanced ω_s during descent. Vertical stretching subsequently causes rapid intensification after the parcels enter the convergence zone along the vorticity river, similar to the case of vorticity river A.

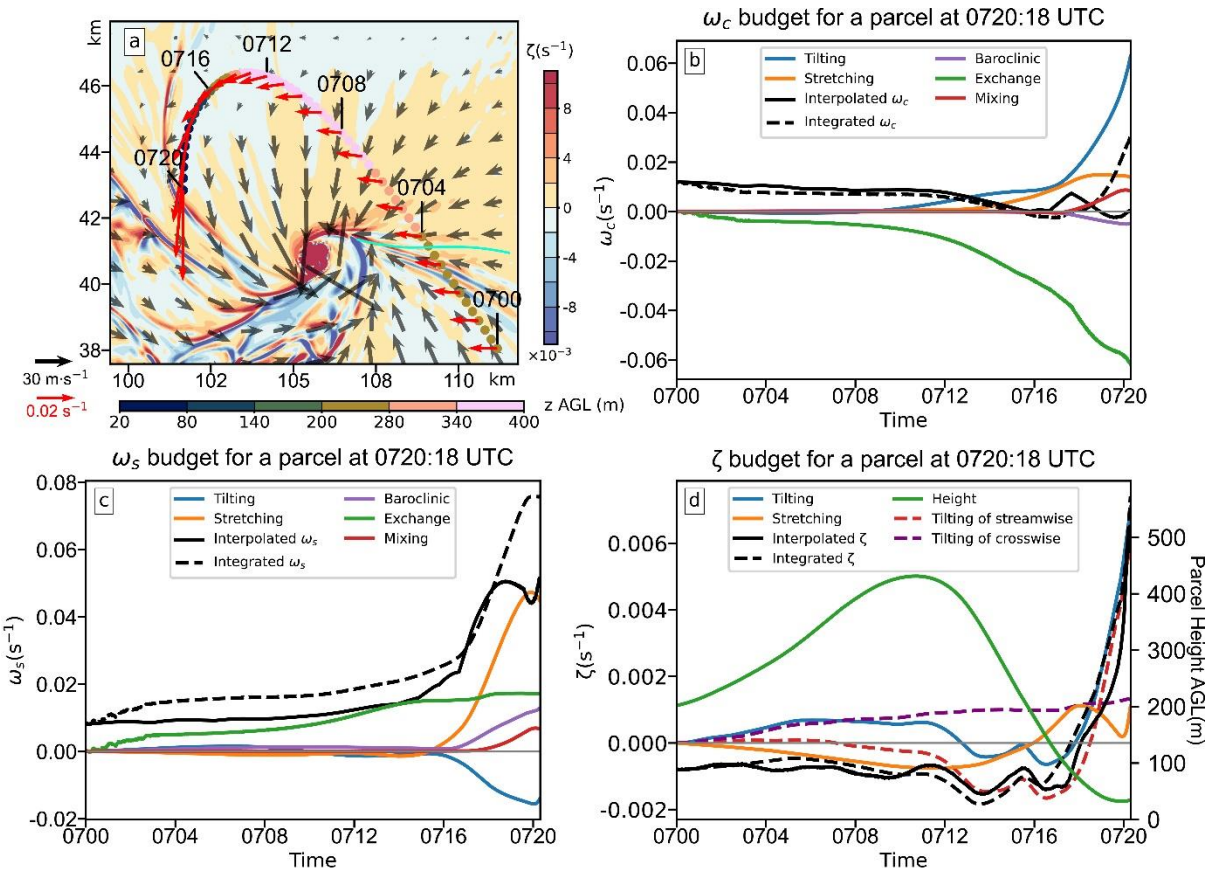

Fig. 4. As in Fig. 3, but the horizontal vorticity vectors (red arrows, s^{-1}) are plotted at 60 s intervals for a representative backward trajectory that terminates at ~35 m AGL in vorticity river B at 0720:18 UTC.

The representative trajectory of the parcel entering vorticity river C also originates from the inflow region and moves northwestward at first then turns southward, similar to the trajectories with vorticity rivers A and B (Fig. 5a). Again, the parcel possesses

Accepted for publication in *Journal of the Atmospheric Sciences*. DOI 10.1175/JAS-D-24-0227.1.

significant ω_c (~0.022 s^{-1}) and ω_s (~0.016 s^{-1}) at the beginning, and the horizontal vorticity vectors point towards the forward-left direction of the trajectory.

The parcel first ascends from ~150 m to ~230 m AGL between 0700 to 0713 UTC, then descends to ~15 m AGL by 0724 UTC (Fig. 5d) when it enters vorticity river C (Fig. 5a). For converting ω_c to ω_s, the exchange terms between them are most significant before 0718 UTC when the trajectory turns leftwards. ω_s rapidly increases through stretching after 0718 UTC when the parcel accelerates towards the tornadic region (Fig. 5c). Both frictional and baroclinic generations of horizontal vorticity are very small, as with vorticity rivers A and B, except for the increase of the frictional term after 0720 UTC.

Vertical vorticity ζ does not change much before 0714 UTC when the parcel reaches its maximum height (Fig. 5d). It then decreases and turns negative mostly due to the downward tilting of ω_s as the parcel descends. In the process, stretching contributes positively by decreasing the magnitude of the negative ζ (increasing ζ) via vertical compression. As the downward trajectory reaches its inflection point when its slope starts to decrease at 0719 UTC, the stretching term turns negative (as the parcel decelerates towards the ground). Meanwhile, the tilting term, particularly the tilting of, first generated by conversion from crosswise and then by stretching induced horizontally accelerating southward flow, starts to make a significant positive contribution, leading to positive integrated ζ by 0722 UTC. After 0724 UTC, when the parcel reaches its nadir and starts to rise, large ζ is produced via vertical stretching and tilting of ω_s for it to reach ~0.01 s^{-1} within about 1 minute. Therefore, the overall evolution is very similar to those of vorticity rivers A and B.

Accepted for publication in *Journal of the Atmospheric Sciences*. DOI 10.1175/JAS-D-24-0227.1.

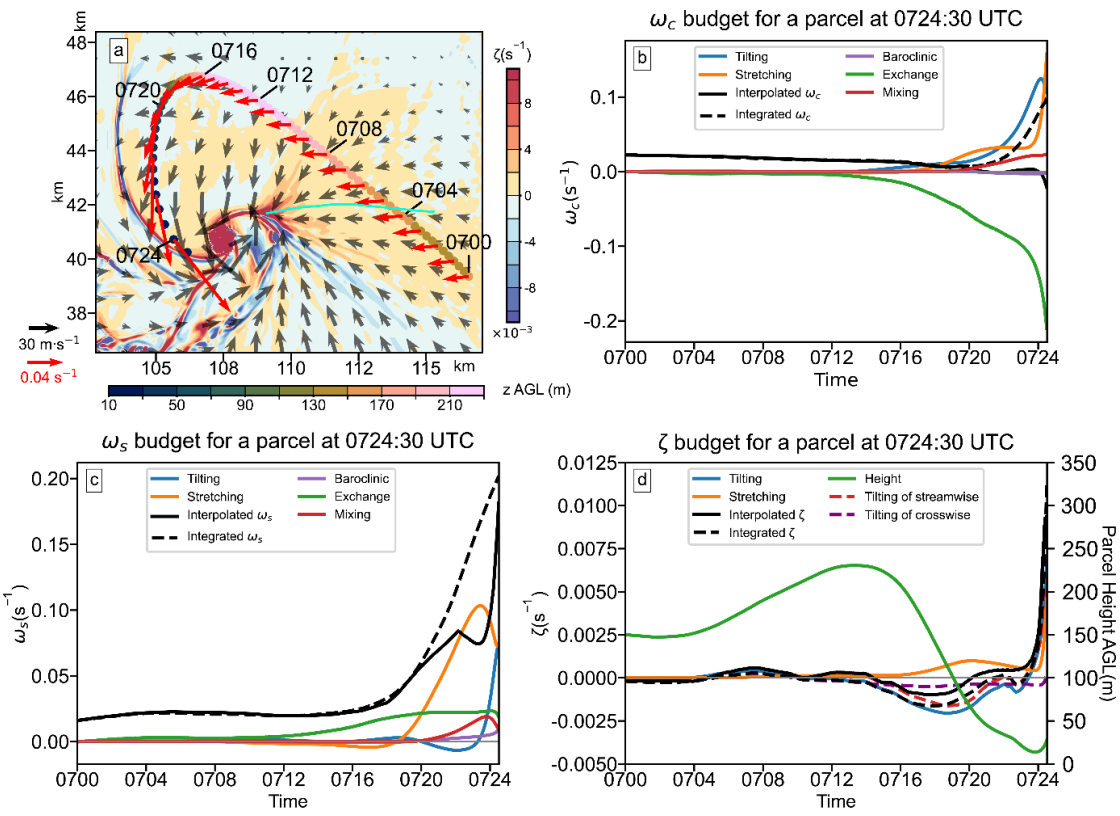

Fig. 5. As in Fig. 3, but the horizontal vorticity vectors (red arrows, s^{-1}) are plotted at 60 s intervals for a representative backward trajectory that terminates at ~27 m AGL in vorticity river C at 0724:30 UTC.

Overall, the budgets of horizontal vorticity components along the trajectories entering the three vorticity rivers share many common aspects. At the beginning of the calculated parcel trajectories, there exists a significant amount of quasi-horizontal vorticity with the crosswise component being larger than the streamwise component, and with the vorticity vector pointing to the left of the parcel track. This vorticity is most likely generated by surface friction as the parcel accelerates into the storm or is contained in the near-surface shear of the environmental sounding that is often called barotropic vorticity (Dahl et al. 2014). The conversion of ω_c to ω_s occurs due to the river-bend effect when the parcels turn from the northwestward to southward directions. Horizontal streamwise vorticity is then dramatically enhanced by horizontal stretching after parcels turn and accelerate southward towards the tornado vortex. The conversion of crosswise to streamwise vorticity and subsequent horizontal stretching play similar roles as baroclinic horizontal vorticity generation in the DJB mechanism during descent.

Accepted for publication in *Journal of the Atmospheric Sciences*. DOI 10.1175/JAS-D-24-0227.1.

Frictional and baroclinic terms play minor roles in producing horizontal vorticity during the trajectory analysis period.

For vertical vorticity, the initial tilting of horizontal vorticity, mostly of ω_s, has a negative contribution to ζ, as ω_s is turned downward by the descending trajectories. Vertical vorticity during this period is mostly negative. After the descending parcel trajectory passes through its inflection point so that its slope decreases, the tilting of ω_s enhanced by conversion from ω_c to ω_s and then through stretching by the southward accelerating flow, becomes positive and starts to increase ζ rather rapidly before the nadir is reached. After the parcel passes the nadir and begins to ascend when it enters the convergence region along the vorticity river, vertical vorticity is rapidly amplified by vertical stretching and further tilting of horizontal vorticity. In the following subsection, we will further investigate the causes of the sinking and then rising motions along the trajectories, given their importance to the vorticity evolution.

c. Vertical motions near and at the vorticity rivers

During the final minute of the trajectories associated with the three vorticity rivers, the updraft along the vorticity rivers is critical for the formation of vorticity rivers because it provides strong upward tilting of horizontal vorticity and stretching of vertical vorticity. Earlier, we suggest that the updraft is caused by horizontal convergence from the sides of the rivers. To better understand the cause, vertical velocity and related wind fields at ~26 m AGL and in vertical cross-sections across the vorticity rivers are plotted in Fig. 6. The times chosen for plotting are slightly earlier than the times when vorticity rivers have fully formed. There exist easterly winds on the east side of vorticity rivers at 26 m AGL (Fig. 6a–c). The easterly winds accelerate towards the locations of the vorticity rivers and weaken quickly as the flow reaches the location of the vorticity rivers. The winds west of the vorticity rivers are more turbulent and weaker with weak northeasterly or even westerly. Such wind distributions lead to strong horizontal convergence (c.f. Fig. 1b–d) and force upward motion at the location of vorticity rivers (Fig. 6a–c).

Along each vorticity river is a narrow band of strong updraft, while downdrafts on both sides are seen in the horizontal cross sections (Fig. 6a–c). The downdrafts can also be seen in the vertical cross sections (Fig. 6d–f). The strong descending motion is found

Accepted for publication in *Journal of the Atmospheric Sciences*. DOI 10.1175/JAS-D-24-0227.1.

extending from the surface to 2 km AGL or higher on two sides of the rivers. When the downdrafts reach the surface, the airflows have to spread out. The stronger downdraft on the east side would generate stronger easterly winds near the ground compared to the west side of the rivers (Fig. 6a–c). This results in strong horizontal convergence (c.f. Fig. 1b–d), which in turn forces upward motion at the locations of vorticity rivers (Fig. 6a–c). As a result, ascent is found to extend from the surface to heights between 750 and 1500 m AGL at the river locations (Fig. 6d–f). Such ascending motion is responsible for the strong tilting of horizontal vorticity into vertical in the final minute of the trajectories.

As the downdrafts on the east side of rivers approach the ground, warm air pockets develop, as inferred from 0.8 K of θ_ρ' (c.f. Fig. 1b–d). The warm air is then pushed by the cyclonically rotating convergent winds towards the tornado vortex, resulting in a higher θ_ρ' immediately behind the RFGF (e.g., 0711:00 and 0720:18 UTC; Fig. 1b and c). The higher θ_ρ' associated with the downdrafts (Fig. 1) suggests that the forcing driving the downdraft is likely dynamic rather than thermodynamic. Additionally, the similar θ_ρ' values between the two sides of the vorticity rivers imply that the origins of air masses on both sides are similar.

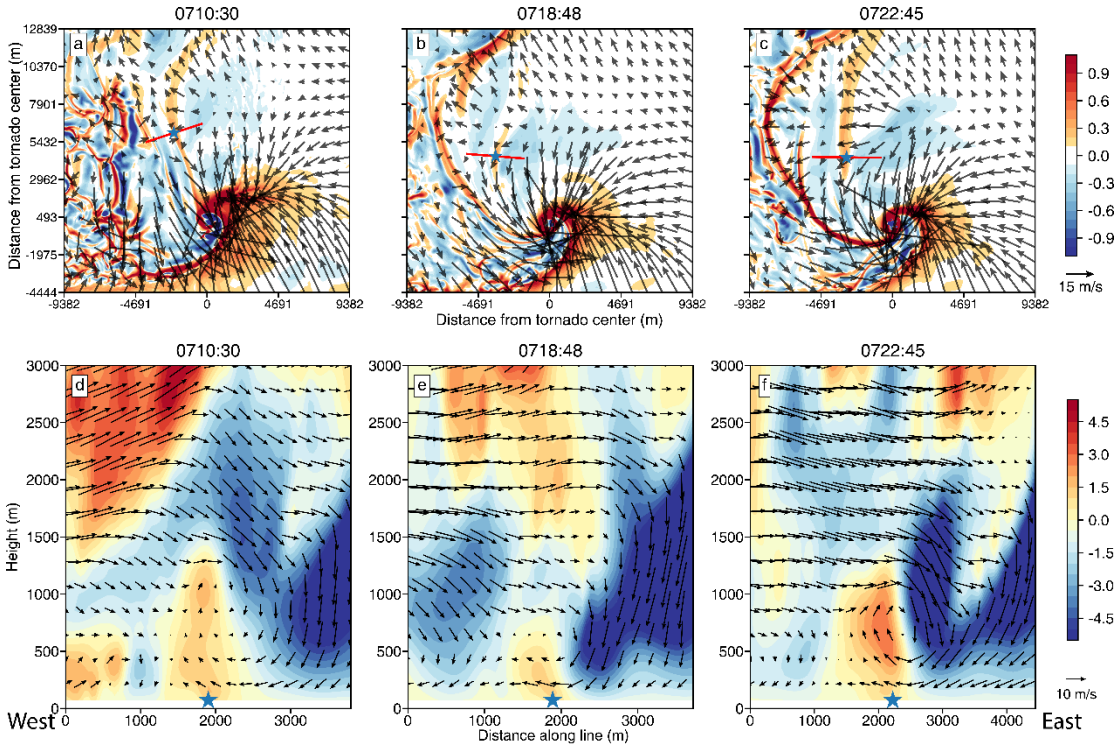

Accepted for publication in *Journal of the Atmospheric Sciences*. DOI 10.1175/JAS-D-24-0227.1.

Fig. 6. Vertical velocity (shaded; m s^{-1}) and ground-relative wind vectors (m s^{-1}) associated with the three vorticity rivers at 26 m AGL at (a) 0710:30, at (b) 0718:48, and at (c) 0722:45 UTC. The red straight lines in (a), (b), and (c) indicate the positions of vertical cross sections of vertical velocity and wind vectors from west to east shown in (d)–(f). The blue star indicates the position of the vorticity river in each panel.

The downdrafts of different intensities on the two sides of the rivers that create surface convergence are clearly important. To better understand the process, we calculate backward trajectories similar to those in section 3b but focus on the parcels on the sides of and along the vorticity rivers at their initiation times.

We take the vorticity river C as an example to show the results of the backward trajectory analysis. The results with vorticity rivers A and B are similar. The parcels are initiated at ~ 37 m AGL at 0722:45 UTC. Parcels all come from the region south of the FFCB where weak rising motion exists (Fig. 7a). The initial locations of parcels ending up on the west side of vorticity river C have westward locations that are closer to the tornadic region, while those parcels ending up on the east side of the river are farther away from the tornado region at the beginning. The parcels initially move northwestward and ascend somewhat (Fig. 7a–b). From 0713:09 UTC, when entering a downdraft region north of FFCB, the parcels begin to turn from northwestwards to southwestwards and descend (Fig. 7c–d). After 0718:48 UTC, the parcels continue to descend more quickly and further turn left towards the tornado convergence center (Fig. 7e). When approaching the ground, the airflows associated with parcels that end up on both sides of the river induce surface convergence, leading to rising motion at the location of the river near the ground (Fig. 6f). The downward turning of the trajectories should be a part of the broader forward-flank downdraft in that region.

Accepted for publication in *Journal of the Atmospheric Sciences*. DOI 10.1175/JAS-D-24-0227.1.

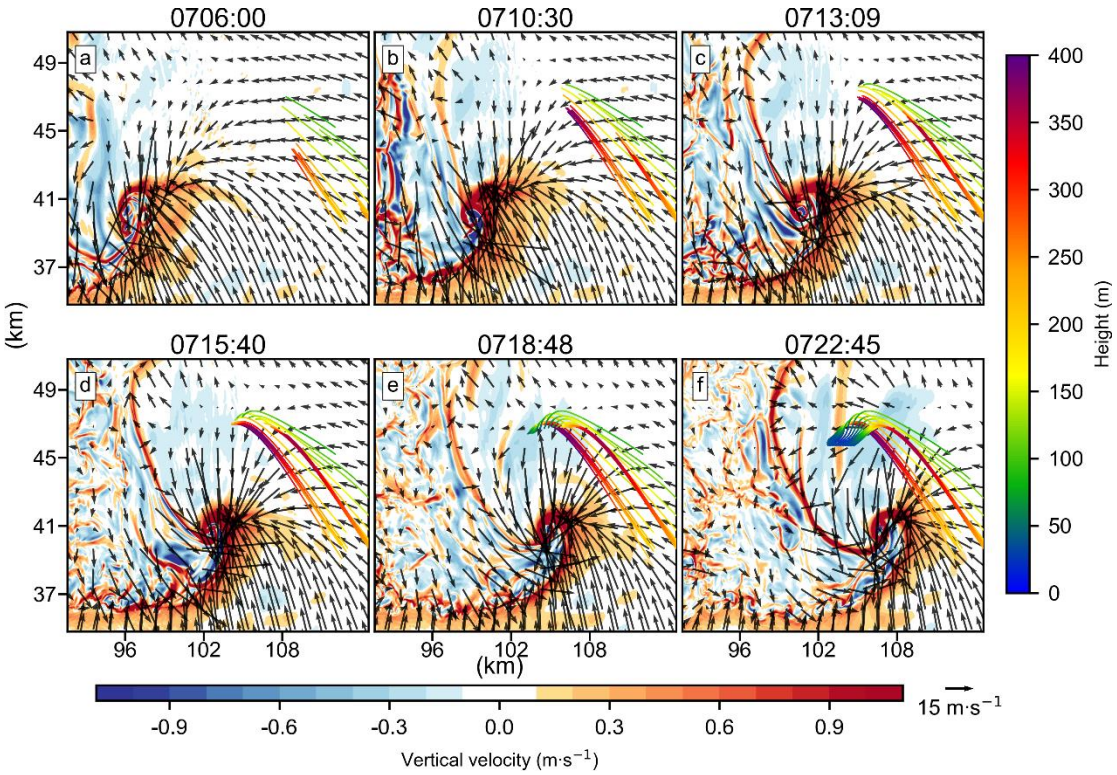

Fig. 7. Backward trajectories that terminate at ~43 m AGL at 0722:45 UTC focused on the parcels on two sides of and along vorticity river C. Trajectory height (colored lines, m AGL) is plotted at 1-s increment. The trajectory is overlaid with the ground-relative horizontal wind vectors (m s^{-1}) and vertical velocity at ~ 43 m AGL (shaded, m s^{-1}).

4. The influxes of vorticities into the tornadic region

As discussed earlier, vorticity rivers are connected to the tornado vortex, and the ingestion of positive vertical vorticity contained within these rivers may contribute to tornado intensification or maintenance. In the in-and-up mechanism, as advocated in Fischer and Dahl (2022), ground-level vertical vorticity can be generated by the sudden tilting of horizontal vorticity into the vertical, which is then intensified by stretching. In this respect, horizontal vorticity contained in the vorticity river may also play an important role in tornado intensification and maintenance. In this section, we calculate the fluxes of vertical and horizontal vorticity advected into the tornadic region from different directions, and quantify the relative contribution from the vorticity rivers.

a. Vorticity fluxes into the tornadic region

Accepted for publication in *Journal of the Atmospheric Sciences*. DOI 10.1175/JAS-D-24-0227.1.

To quantitatively determine the contribution of vorticity in the vorticity rivers to the tornado, we calculate horizontal and vertical vorticity fluxes through a circle of unit height, at ~26 m AGL where the strongest vertical vorticity is found in the simulated tornado (Fig. 2 and Fig. 8). The circle for the budget calculations is chosen so that it is not too far from the center of tornado but also large enough to capture the vorticity coming in from all directions.

Figures 2 and 8 show that there are two main regions with the most significant influxes of vertical and horizontal vorticity into the tornadic region. One is associated with the zone between the occluded RFGF and FFCB located on the north and northeast side of the tornado vortex (e.g., Fig. 2i). Here, the occlusion zone refers to the occluded front or convergence zone between RFGF and FFCB, which can be seen in the form of a narrowly enhanced band of vertical vorticity more clearly after 07:20:18 UTC in Fig. 2 (panels i through l). Another region with significant vorticity influxes is where the vorticity rivers enter the tornadic region. The slight mismatch between the positions of the vorticity rivers and the strong vorticity influxes (e.g., at 0718:48 UTC; Fig. 2h and Fig. 8h) is because the vorticity inflow intensity depends on the vorticity and radial inflow. The stronger radial wind along the occlusion zone results in stronger vertical vorticity influx than the vorticity rivers, although the vertical vorticity associated with the occlusion zone is smaller than the vorticity rivers (Fig. 2).

The low-level vertical vorticity band at the occlusion zone is much narrower (Fig. 2) than the horizontal vorticity band (Fig. 8). The horizontal vorticity band can become rather broad at the later stage (Fig. 8). The narrow band of vertical vorticity of the occlusion zone (Fig. 2) corresponds well to the northern boundary of the broader horizontal vorticity spiraling into the tornado vortex (Fig. 8), suggesting that the vertical vorticity entering the tornado vortex originates to a large extent from the tilting of the horizontal vorticity converging into the occlusion zone. The distribution of vertical vorticity is non-uniform, especially at earlier times (Fig. 2a–c), therefore, the radial influx of ζ exhibits discontinuities along the circle.

Accepted for publication in *Journal of the Atmospheric Sciences*. DOI 10.1175/JAS-D-24-0227.1.

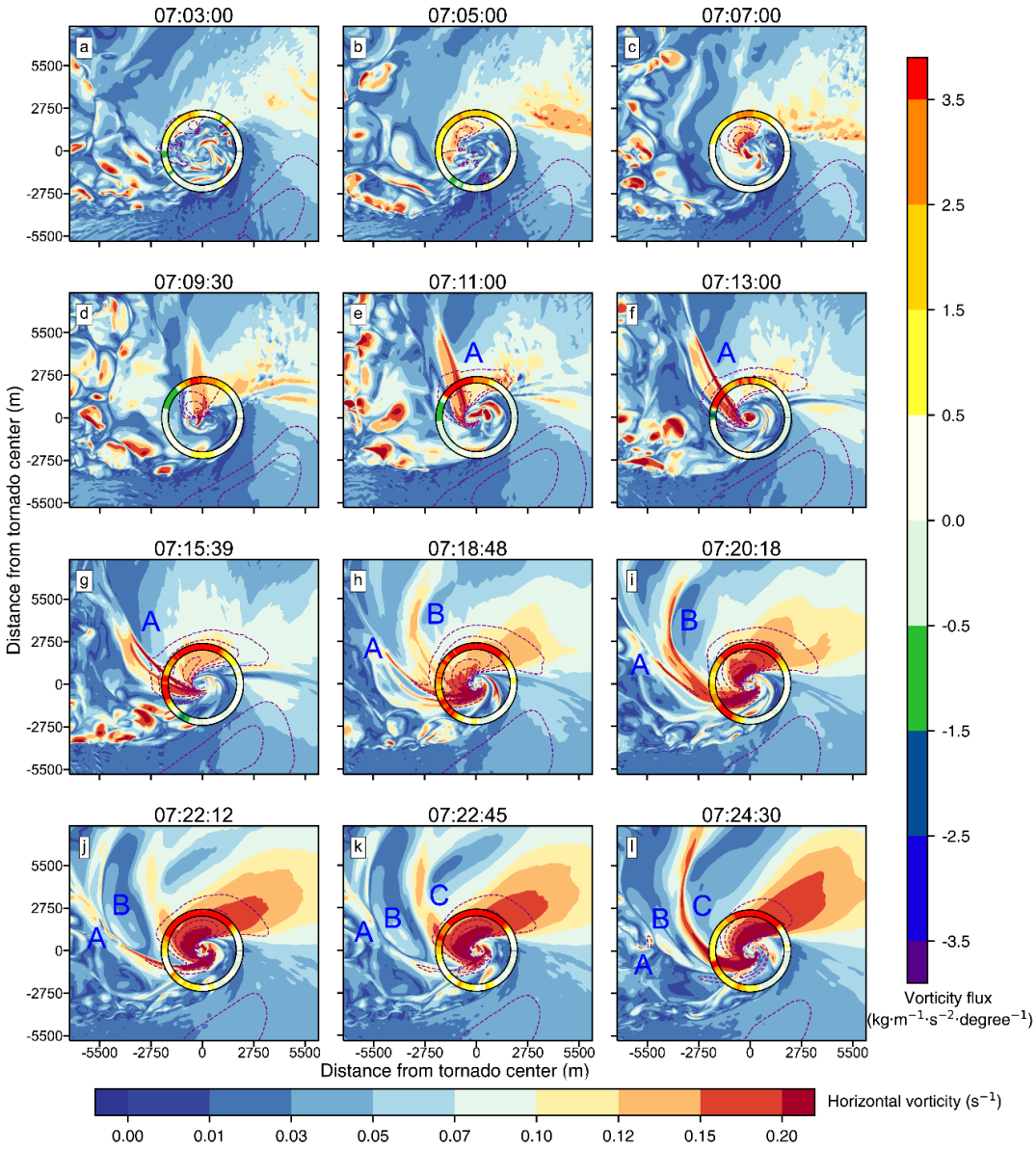

Fig. 8. Similar to Fig. 2, but for horizontal vorticity (shaded, s^{-1}), overlaid with radial wind (dashed contours at 20, 25, 30, 35, 40 m s^{-1}) and radial flux of horizontal vorticity through a circle of 1 meter high (shaded line; kg m^{-1} s^{-2} $degree^{-1}$) at ~26 m AGL.

We further use time-azimuth Hovmöller diagrams to show the time evolution of radial influxes of horizontal and vertical vorticity, in terms of vorticity flux per unit azimuthal degree angle through the circle. Here, the influx is calculated over a wall that is 150 m tall, based on the formula - $\int_{sfc}^{150m} \rho V_r \zeta \, dz$, where ρ, V_r and ζ are the air density, radial velocity, and vertical or horizontal vorticity, respectively. The 150 m depth of the 'flux wall' encompasses the depth of the vorticity river and accounts for

Accepted for publication in *Journal of the Atmospheric Sciences*. DOI 10.1175/JAS-D-24-0227.1.

the most important influxes of vorticity into the tornadic region. The influxes of vorticity associated with the occlusion zone and vorticity rivers and their time evolution can be seen clearly in the Hovmöller diagrams (Fig. 9). For vertical vorticity, the influxes from the occlusion zone northeast of the tornado are intermittent between 0702:00 and 0710:00 UTC but become stronger though still somewhat intermittent between 0710:00 and 0715:00 UTC (Fig. 9a), corresponding to somewhat disorganized vertical vorticity structures in the region (see Fig. 2a–f). After 0715:00 UTC, the positive influx from the northeast becomes much more persistent and stronger (Fig. 9a), consistent with ζ being almost uniformly positive along the occlusion zone (Fig. 2g–l). The influx of horizontal vorticity coming from the northside is consistently positive and is also stronger and broader after 0710 UTC (Fig. 9b), and it is accompanied by a significant broadening in azimuthal range in the region of strong horizontal vorticity near the flux circle (Fig. 8).

In the Hovmöller diagrams, the vorticity influxes associated with the vorticity rivers show up as much narrower bands whose positions rotate counterclockwise from the north or northwest side to the west and eventually the south side of the tornado vortex as indicated by the thick arrowed blue lines in Fig. 9. Before 0710 UTC, there is no clear vorticity influx that rotates counterclockwise. The most noticeable and robust band is associated with vorticity river A. It is first seen on the north side of the tornado vortex at ~0710, then rotates counterclockwise, slows down at ~0721 UTC, and finally stalls on the south side of the tornado at ~0725 UTC. The second weaker band of vorticity influx associated with vorticity river B also rotates counterclockwise and eventually merges with that of vorticity river A around 0724 UTC. The third band associated with vorticity river C appears evident later and again rotates counterclockwise and becomes stagnant on the south side of the tornado vortex.

When comparing the vorticity influxes along the occlusion zone and the vorticity rivers, the vorticity influx along the occlusion zone is much greater in magnitude for both vertical and horizontal vorticity (note the color palette differences in Fig. 9). The fact that the width of vorticity rivers is much narrower than the occlusion zone further limits the vorticity influx of transported by the rivers.

The influx of horizontal vorticity is an order of magnitude larger than that of vertical vorticity ζ (Fig. 9) because the magnitude of horizontal vorticity is larger than ζ (Fig.

Accepted for publication in *Journal of the Atmospheric Sciences*. DOI 10.1175/JAS-D-24-0227.1.

2 and Fig. 8). These results emphasize that both the occlusion zone and vorticity rivers help strengthen and maintain tornadoes primarily by transporting horizontal vorticity into the tornadic region and the in-and-up mechanism (Fischer and Dahl 2022) is likely playing the dominant role (at these times after tornadogenesis at least) while the influx of vertical vorticity only plays a secondary role. The majority of the vorticity influx is from the occlusion zone, while the influx due to the vorticity rivers is small because of their narrower width and shallower depth.

The position of large influxes of horizontal vorticity along the occluded zone in our study is similar to that of streamwise vorticity current (SVC). The SVC as a region with enhanced horizontal streamwise vorticity on the cold side of the FFCB has been identified by previous simulations and observations (Beck and Weiss 2013; Orf et al. 2017; Murdzek et al. 2020; Schueth et al. 2021; Finley et al. 2023). These studies pointed out that the horizontal vorticity along the SVC is mainly generated baroclinically. Schueth et al. (2021) further found that the maximized streamwise vorticity occurred in the center of Kelvin-Helmholtz billow forming along the gust front where strong θ_ρ' gradient exists. The baroclinically generated horizontal vorticity can be further stretched by the axial inflow towards the tornado vortex, resulting in even stronger streamwise vorticity within the SVC. In our case, however, the θ_ρ' gradient is weak across FFCB (c.f. Fig. 1). An important distinction between our and their simulations is the inclusion of surface friction in our simulation, which can generate large crosswise horizontal vorticity that can become streamwise as discussed earlier, especially at heights close to the ground.

Accepted for publication in *Journal of the Atmospheric Sciences*. DOI 10.1175/JAS-D-24-0227.1.

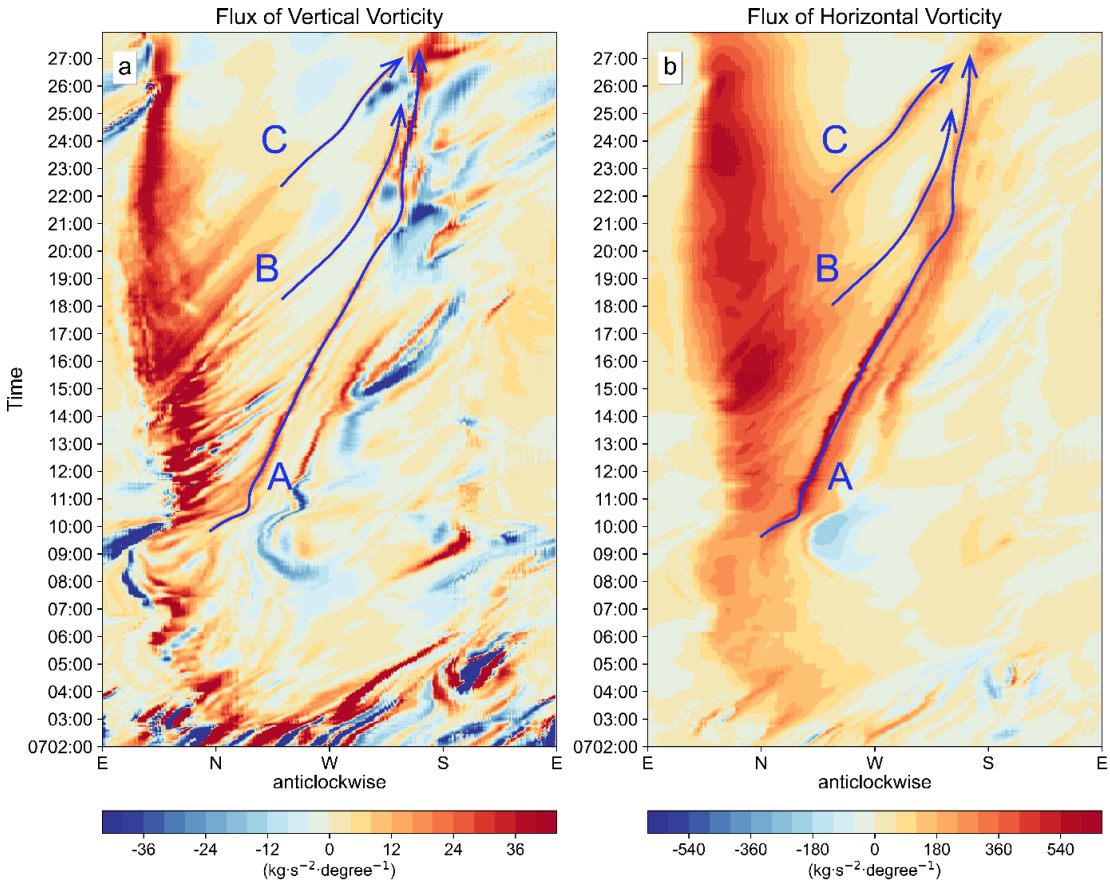

Fig. 9. The time-azimuth angle (azimuth is 0º due east and 90º due north) Hovmöller diagrams of radial influxes of (a) vertical vorticity (shaded, kg s^{-2} $degree^{-1}$) and (b) horizontal vorticity (shaded, kg s^{-2} $degree^{-1}$) integrated from surface to ~ 150 m at the radius of the circle in Fig. 8 from 0702:00 to 0727:57 UTC (07 is omitted in the vertical axis labels). Positive values indicate an inflow of vorticity into the tornado. The horizontal axis points in the counterclockwise direction. The 'ridge lines' of local maximum vorticity influx are marked by thick blue arrowed lines, corresponding to vorticity rivers A, B, and C.

b. Parcel trajectories into the tornadic region

The above analyses are conducted in Eulerian coordinates. We also perform an analysis in Lagrangian coordinates to find out how many parcels that finally enter the tornadic region actually pass through the vorticity rivers. We take the parcels entering vorticity river C as an example. The results for rivers A and B are similar.

At 0724:30 UTC, the tornado is mature, and the strongest vorticity is near the ground. We initialize 1681 parcels at ~26 m AGL at 50 m spacing within a 2 km by 2 km box at 0724:30 UTC to cover the tornadic region and integrate them backward in time to 0700 UTC. Only parcels with vertical vorticity greater than 0.01 s^{-1} at 0724:30

Accepted for publication in *Journal of the Atmospheric Sciences*. DOI 10.1175/JAS-D-24-0227.1.

UTC are considered, yielding a total of 711 parcels. These parcels are subjectively categorized into six groups according to the initial positions and the distribution of the trajectories in the horizontal projection, as shown in Fig. 10. The trajectories of groups 1–3 are similar, with all parcels moving northwestward from the inflow region south of FFCB, then turning southward and finally entering the tornado from the north or northwest side of the tornado. These parcels remain below 500 m in height throughout the time. Trajectories in Group 1 are largest in number, totaling 510, representing approximately 72% of the total, and they mostly enter the tornado from the north side through the occlusion region (see supplementary material for animations).

The initial (earliest time) east-west positions of trajectories of Group 2 ($x \approx 84000$ m) are closer to the initial position of the tornado vortex ($x \approx 63000$ m) than those of Group 1 ($x \approx 87000$ m). Group 2 ranks second in parcel count, with 66 parcels, making up 9% of the total. The positions of Group 3 trajectories lie between those of Groups 1 and 2. The parcels of Group 3 are those that move along vorticity river C and finally enter the tornadic region. Note that although the trajectories of Group 2 seem more consistent with the position of the vorticity river at the time shown in Fig. 10, those trajectories do not actually flow along vorticity river C. The vorticity river and Group 2 trajectories only seem to coincide at the time shown. The animation of trajectories shows that Group 3 trajectories move along the vorticity river C and finally enter the tornado vortex, while Group 2 trajectories merely pass through the vorticity river (see supplementary material for animations). The vorticity rivers are not stationary, they would rotate cyclonically with time. Group 3 comprises 49 parcels, accounting for 7% of the total; this is consistent with the fact that the vorticity river is rather narrow. This further substantiates the earlier results that, while a vorticity river may have some impact on tornado intensification and maintenance, any impact would be limited. The parcels of Group 4, having 50 parcels, originate from the inflow region of the tornado south of the FFCB. However, their initial east-west positions ($x < 79{,}000$ m) are much closer to the tornado vortex ($x \approx 63000$ m) compared to the trajectories in Groups 1–3 ($x > 83000$ m). Group 5 with 7 parcels is from the RFGF, and the parcels are ingested into the tornado vortex and then descend while spiraling around the tornado (see supplementary material for animations). Therefore, the trajectories of Group 5 exhibit spiral paths in the horizontal projection. The 29 parcels in Group 6 also originate from the RFGF but are drawn into the tornado vortex from the south.

Accepted for publication in *Journal of the Atmospheric Sciences*. DOI 10.1175/JAS-D-24-0227.1.

The above results show that the majority of parcels entering the tornado are from the inflow region of the supercell south of the FFCB. Very few parcels flow through the vorticity rivers before entering the tornadic region, partly because of their narrow width. This is consistent with the results of the vorticity influx budget calculations. Although vorticity rivers can transport horizontal and vertical vorticity into the tornadic region, the narrow width of vorticity rivers limits their overall contribution in terms of vorticity budget. This finding is consistent with those of Beck and Weiss (2013), who also found that only a small fraction of parcels passed through vorticity rivers (called LFCB in their study) before entering the low-level rotation region. Somewhat differently, Sherburn and Parker (2019) noted in their simulation using a 250 m horizontal spacing for a high-shear, low-CAPE environment that most of the parcels feeding the tornado came from the north or northeast side, where vorticity river-like structures are present. However, they did not perform any quantitative analysis on the relative contributions of vorticity rivers.

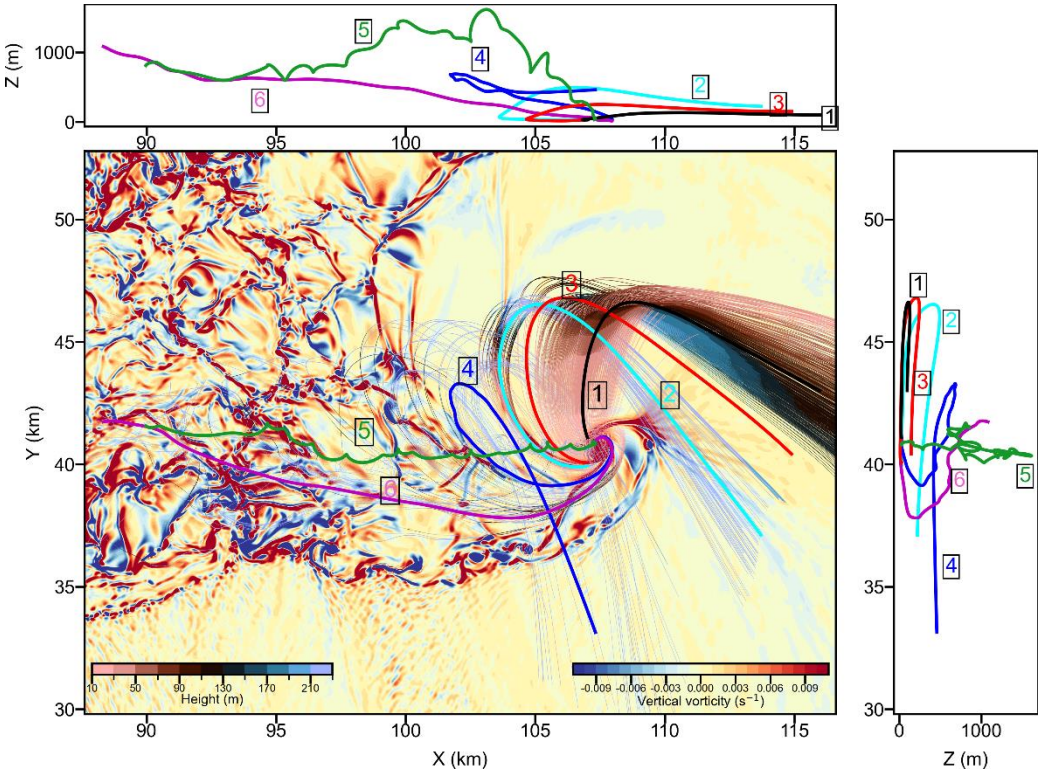

Fig. 10. The trajectory that parcels enter the tornado vortex at 0724:30 UTC overlaid with vertical vorticity (shaded, s^{-1}). The shades of thin lines represent the height of parcels. Black, cyan, red, blue, green, and purple bold lines indicate the average paths of trajectories 1, 2, 3, 4, 5, and 6, respectively. For clarity, only the average trajectories of 6 groups are shown in X-Z (top panel) and X-Y projections (right panel).

Accepted for publication in *Journal of the Atmospheric Sciences*. DOI 10.1175/JAS-D-24-0227.1.

Finally, we point out that the trajectories presented in Fig. 10 are initialized from within the low-level tornado vortex and integrated backward in time using a fourth-order Runge–Kutta time integration scheme (Schenkman et al. 2012) and model output at 1 s intervals. Initializing the trajectories this way guarantees that we will obtain trajectories ending within the tornado vortex. Dahl et al. (2012) suggested that there may be more uncertainties or errors in trajectories integrated backward in time in strongly confluent flows. For forward trajectories converging into a small-scale vortex with large flow curvature, larger errors often occur near the end of the trajectory calculation as they converge into the vortex. When the trajectories are calculated backward in time from the vortex region, the errors occurring near the beginning of the calculation (where flow curvature is large) can lead to large errors in the trajectory positions at the earlier times. To examine the potential issues with the background trajectories presented in the Fig. 10, we integrated a set of trajectories forward in time, starting from the parcel positions at 0709:54 UTC of the backward trajectories, i.e., of those shown in Fig. 10. The forward trajectories are integrated through 0725:30 UTC to allow for some differences in the timing when the parcels enter the tornado vortex region. Because many of the backward trajectory parcels are out of the boundary of the innermost simulation domain at 0700:00 UTC, the initial time is chosen to be 0709:54 UTC when all 1681 parcels of the backward trajectories are within the innermost simulation domain. Only parcels with vertical vorticity greater than 0.01 s^{-1} at 0725:30 UTC are considered, with a total of 702 parcels meeting this criterion. Using a grouping method similar to that of the backward trajectories, Group 1 of the forward trajectories has 379 parcels, accounting for 54% of the total number. Groups 2 and 3 have 19 and 51 trajectories, accounting for 3% and 7% of the total, respectively. Groups 4, 5, and 6 have 122, 27, and 104 trajectories, respectively.

Comparing the parcel numbers in each group between forward and backward trajectories, the number in Group 1 is smaller than that of the backward trajectories, while the numbers in Groups 4–6 are slightly larger than those of the backward trajectories. Group 3 trajectories, which pass through vorticity river C and finally enter the tornado, are similar to those of the backward trajectories. Additionally, the horizontal projections of trajectories of all six groups are similar in general distribution

Accepted for publication in *Journal of the Atmospheric Sciences*. DOI 10.1175/JAS-D-24-0227.1.

and pattern between forward (Fig. 11) and backward trajectories (Fig. 10), except that Group 5 trajectories do not reach the ground at 0725:30 UTC. These results indicate that the trajectories calculated forward or backward in time are at least qualitatively similar. The relatively small differences between forward and backward trajectories may have benefited from the high temporal resolution of the velocity data (1-second interval) used in the trajectory calculations.

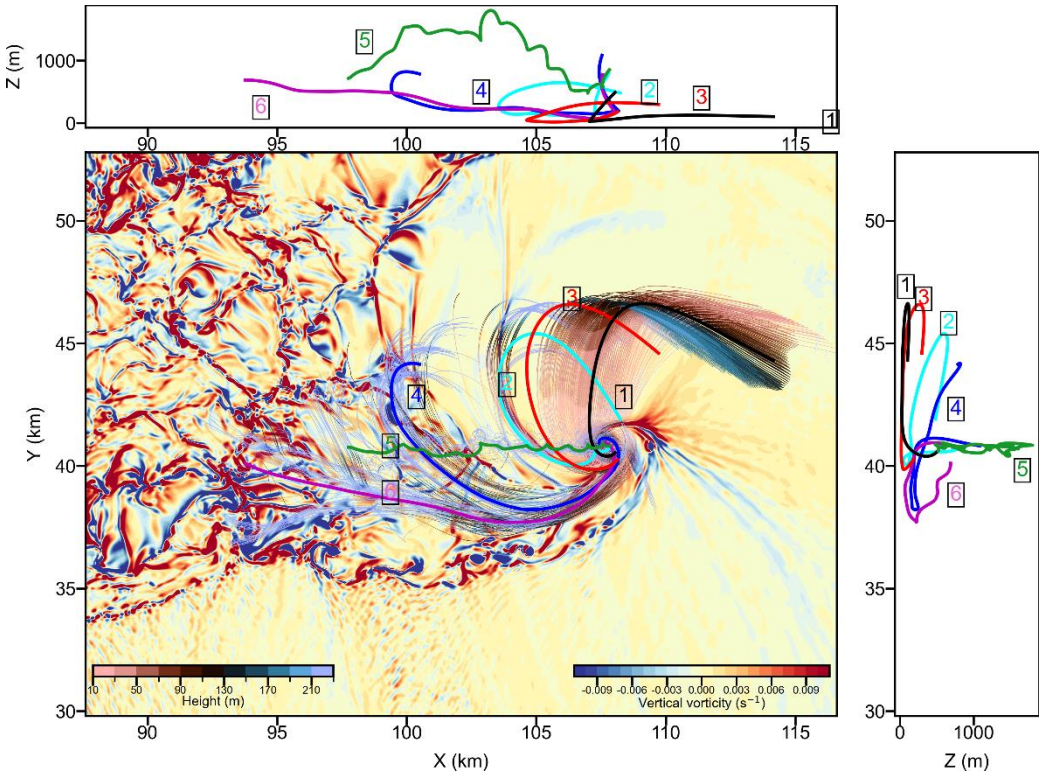

Fig. 11 Same as Fig. 10, but for trajectories initialized at 0709:54 UTC, at the locations of the backward trajectories shown in Fig. 10, and integrated forward in time to 0725:30 UTC.

5. Summary and discussions

An EF4-intensity tornado occurred in Funing County, Jiangsu Province, China, on 23 June 2016. Sun et al. (2019) successfully simulated the life cycle of the tornado using five nested grids with the innermost grid having a 49 m grid spacing. The tornadogenesis occurs at 0703:20 UTC in the simulation, with the maximum vorticity found at the surface. The intensity of the tornado further increases after 0707:00 UTC and reaches its maximum surface vertical vorticity around 0724:00 UTC. During the intensification and mature stages of the tornado, three successive vorticity rivers

Accepted for publication in *Journal of the Atmospheric Sciences*. DOI 10.1175/JAS-D-24-0227.1.

containing narrow bands of positive vertical vorticity are produced. The vorticity river is defined as a near-ground vertical vorticity band extending from the regions north side of simulated supercells towards an intensifying or a mature tornado. The three vorticity rivers all rotate counterclockwise, stall on the south side of the tornado, and eventually merge together and vanish. The vorticity rivers are generally found where the left flank convergence boundary (LFCB) is in simulated supercells (Beck and Weiss 2013), and have been suggested to be similar in nature to LFCB.

The key processes for the formation of the three vorticity rivers are analyzed and found to be similar. A conceptual model summarizing the formation mechanism of typical vorticity rivers in supercells is presented in Fig. 12. The air parcels that enter the vorticity river first ascend and move northwestward from the inflow region of the supercell south of FFCB until arriving at the forward-flank downdraft region near vorticity rivers north of FFCB. The horizontal vorticity these parcels carry points generally towards the left-forward direction of the parcel trajectories, indicating significant positive streamwise and leftward pointing crosswise vorticity components. Given the general lack of significant horizontal buoyancy gradient along the tracked parcel trajectories up to this point, the horizontal vorticity likely originates from the inflow environment and may have been enhanced by surface friction when the inflow is closer to the ground before passing over the FFCB.

When the air parcels arrive at the forward-flank downdraft region, they start to descend and turn towards the left, changing from northward to westward and eventually southward directions. Significant conversion of crosswise to streamwise vorticity occurs when the turning occurs due to the river-bend effect. Tilting of horizontal vorticity, mostly of positive streamwise vorticity ω_s, has a negative contribution to vertical vorticity ζ at the beginning of the turning, so that ζ during this period is mostly negative. After the parcels further descend and the slope of the trajectory decreases with decreasing height. The horizontal streamwise vorticity ω_s is increased by exchanging from ω_c and further enhanced by horizontal stretching as the parcels accelerate towards the tornado vortex. The enhanced ω_s introduces "slippage'' between vortex lines and trajectories, therefore can be tilted upward to increase vertical vorticity ζ as the parcels descend with a decreasing slope. The ζ becomes positive before the parcels reach their nadir. When the parcels enter the near-surface convergence region along the vorticity

Accepted for publication in *Journal of the Atmospheric Sciences*. DOI 10.1175/JAS-D-24-0227.1.

river, they begin to ascend rapidly. The convergence along the vorticity river is associated with downdrafts of different intensities on the two sides of the river. Vertical vorticity is rapidly increased by further tilting of horizontal vorticity, especially ω_s and amplification by vertical stretching at the river.

We note here that the formation mechanism of convergence along a LFCB in Beck and Weiss (2013) differs slightly from our findings. They attributed the convergence to different amounts of hydrometeor water content and the resulting density temperature gradient across the LFCB. In our study, however, the density temperature gradient across the vorticity rivers is weak, and the convergence is seen as driven by downdrafts of different intensities on the two sides of the rivers. This suggests that the convergence and the associated vorticity tilting and stretching along the vorticity rivers are primarily induced by dynamic forcing associated with the descending flows rather than buoyancy-induced thermodynamic forcing.

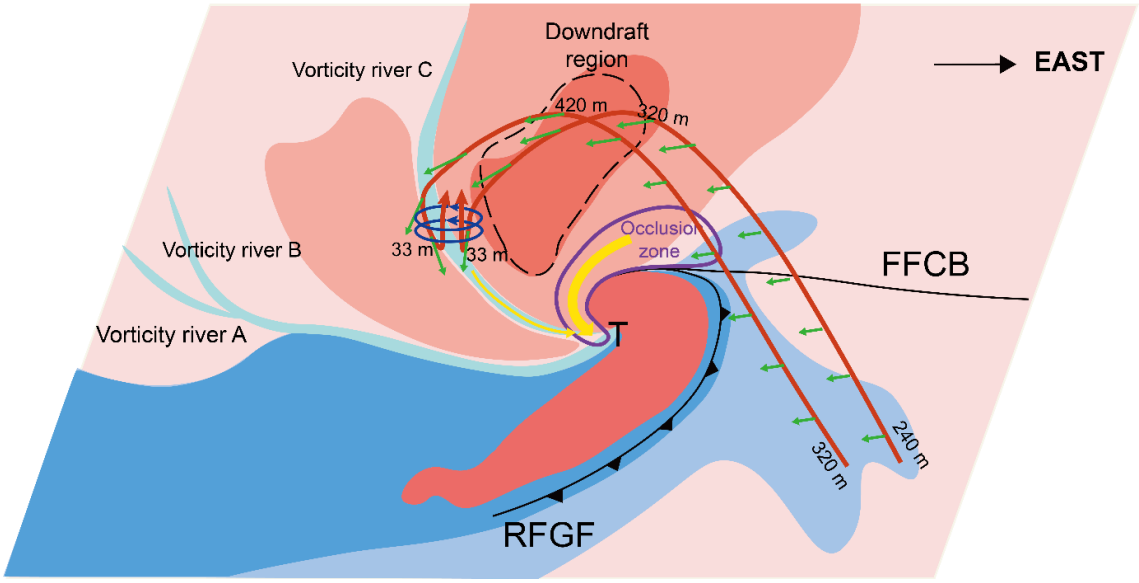

Fig. 12. A schematic showing the formation of a typical surface vorticity river (using vorticity river C in cyan shading as an example) in a simulated supercell storm. The warm (red) and cold (blue) colors on the ground surface indicate positive and negative potential temperature perturbations, respectively. The solid black line with cold front symbols indicates the rear-flank gust front (RFGF), and the black line extending eastward represents the forward-flank convergence boundary (FFCB) with a weak temperature gradient. The warm temperature behind the RFGF and in the downdraft region exists because of dynamically forced downdraft motion, and such warm air is drawn into the tornado. The thick red curves with an arrow at the end represent the two trajectories of air parcels entering the vorticity river from the east and west sides of the river, with the trajectory height labeled in black numbers. The green short vectors indicate the direction of horizontal vorticity along the trajectories. When parcels enter

Accepted for publication in *Journal of the Atmospheric Sciences*. DOI 10.1175/JAS-D-24-0227.1.

the downdraft region, they begin to descend and turn leftward toward the tornado. After the trajectories enter the river at the surface, they rise rapidly from the surface due to convergence along the river, and the horizontal vorticity carried by the parcels is tilted upward, creating positive vertical vorticity along the river. The vertical vorticity is further intensified rapidly by vertical stretching, resulting in a river with a band of significant vertical vorticity. When vorticity river C is fully formed, vorticity rivers A and B, which formed earlier, have merged together at their southern sections and are about to disappear. The occlusion zone between FFCB and RFGF is enclosed by the purple circuit. The yellow curved vectors along the river and in the occlusion zone represent the influx of vorticity into the tornado. The total influx of vertical vorticity from the occlusion zone is much larger than that from the vorticity river due to the deeper depth and larger width of the occlusion zone. Further, in the occlusion zone, the influx of horizontal vorticity is much larger than that of vertical vorticity, suggesting that the in-and-up mechanism of near-surface vertical vorticity generation plays a dominant role at this stage when tornadogenesis has occurred at least.

Horizontal vorticity generated baroclinically or by surface drag is believed to play small roles in the stage of trajectories tracked, which starts immediately before the parcels pass over FFCB until they enter the vorticity river convergence zone. The short trajectory integration time and associated vorticity budget analysis do not exclude potentially significant generation of vorticity by these processes at earlier stages, given that most of the horizontal vorticity, particularly of ω_c, is already present at the beginning of the calculated trajectories. However, since the parcels are in the inflow region south of FFCB, where the temperature gradient is weak, baroclinic vorticity generation is likely small. The significant amount of leftward pointing crosswise vorticity is more likely created by surface drag, either when the parcels are part of the environmental inflow or as the inflow accelerates towards the storm (Roberts et al. 2016). The initial source of the parcel vorticity is not the focus of this paper.

Vorticity rivers possessing vertical and horizontal vorticity are seen to feed into and may have a significant impact on the intensifying and/or mature tornado. The potentially important roles of vorticity rivers in tornadogenesis were suggested by earlier studies (e.g., Dahl et al. 2014), but no previous study has performed a quantitative assessment of their actual roles, including their relative contributions in terms of imported vorticity into the tornadic region. Quantitative calculations of horizontal and vertical vorticity fluxes into the tornadic region in our study reveal two main regions with large vorticity contributions to the tornado. One region is along the occlusion zone between the RFGF and FFCB northeast of the tornado, and another is at the locations of the vorticity rivers. The total amount of vorticity entering the tornadic

Accepted for publication in *Journal of the Atmospheric Sciences*. DOI 10.1175/JAS-D-24-0227.1.

region along the vorticity rivers is less than that entering from the occlusion zone for both vertical and horizontal vorticity, largely due to the narrow width and shallow depth of the vorticity rivers. The backward trajectory analysis for parcels entering the tornado indicates that only about 7% of the parcels move along/through vorticity rivers before entering the tornadic region. These findings suggest that while vorticity rivers may have some impacts on the intensification and maintenance of tornadoes, their direct contribution to tornado intensification and maintenance in terms of vorticity budget is small. Instead, the primary source of both vertical and horizontal vorticity inflow into the tornadic region comes from the occlusion zone on the northeast side of the tornado. In addition, the influx of vertical vorticity is about an order of magnitude smaller than that of horizontal vorticity in general, suggesting the in-and-up mechanism that generates large near-ground vertical vorticity by abruptly tilting horizontal vorticity very close to the intensifying/mature tornado is more important than the influx of vertical vorticity, at least at the stage after tornadogenesis.

So far, field observation of vorticity rivers is generally lacking even though similar structures have been found in a number of simulations (Dahl et al. 2014; Markowski et al. 2014; Coffer and Parker 2017; Coffer et al. 2017; Oliveira et al. 2019; Sherburn and Parker 2019; Snook et al. 2019; Fischer and Dahl 2020). Most simulations are single-sounding-based idealized simulations. Snook et al. (2019) and the simulation in this study are exceptions in that they are real-case simulations with non-flat terrain and non-uniform land surface conditions and include surface drag with non-constant drag coefficients. In these real case simulations using ~50 m grid spacings that are considered large-eddy-resolving, turbulent eddies can develop in the boundary layer when instability exists due to land surface heating and/or strong near-surface wind shear, even though no explicit thermal perturbations are introduced to trigger turbulent eddies (Markowski and Bryan 2016). Markowski (2024) suggests that vertical vorticity streaks developing in a turbulent boundary layer inflow can alter the way tornado-like vortices form in supercell simulations. How such streaks, if they develop in more realistic real-data simulations, may affect vorticity river formation or the most important vorticity supply to the tornado, is a question for future study. In terms of real-world observations, the narrow width and shallow depth of the vorticity rivers make their observation and quantification challenging. The results presented in this paper are based on the numerical simulation of a single tornado case. The results may vary among different

Accepted for publication in *Journal of the Atmospheric Sciences*. DOI 10.1175/JAS-D-24-0227.1.

cases. Observational and numerical studies of additional cases are warranted to test the generality of the conclusions.

Acknowledgements.

This work was primarily supported by NSFC grant 41730965. Zhenqi Sun is acknowledged for making available his simulation configuration and data.

Data Availability Statement.

The data used in this paper can be found at Harvard Dataverse at https://dataverse.harvard.edu/dataset.xhtml?persistentId=doi:10.7910/DVN/DUL5WN&version=DRAFT.

References

Adlerman, E. J., K. K. Droegemeier, and R. Davies-Jones, 1999: A Numerical Simulation of Cyclic Mesocyclogenesis. *J. Atmospheric Sci.*, **56**, 2045–2069, https://doi.org/10.1175/1520-0469(1999)056<2045:ANSOCM>2.0.CO;2.

Beck, J., and C. Weiss, 2013: An Assessment of Low-Level Baroclinity and Vorticity within a Simulated Supercell. *Mon. Weather Rev.*, **141**, 649–669, https://doi.org/10.1175/MWR-D-11-00115.1.

Bluestein, H. B., K. J. Thiem, J. C. Snyder, and J. B. Houser, 2019: Tornadogenesis and Early Tornado Evolution in the El Reno, Oklahoma, Supercell on 31 May 2013. *Mon. Weather Rev.*, **147**, 2045–2066, https://doi.org/10.1175/MWR-D-18-0338.1.

Boyer, C. H., and J. M. L. Dahl, 2020: The Mechanisms Responsible for Large Near-Surface Vertical Vorticity within Simulated Supercells and Quasi-Linear Storms. *Mon. Weather Rev.*, **148**, 4281–4297, https://doi.org/10.1175/MWR-D-20-0082.1.

Coffer, B. E., and M. D. Parker, 2017: Simulated Supercells in Nontornadic and Tornadic VORTEX2 Environments. *Mon. Weather Rev.*, **145**, 149–180, https://doi.org/10.1175/MWR-D-16-0226.1.

Accepted for publication in *Journal of the Atmospheric Sciences*. DOI 10.1175/JAS-D-24-0227.1.

——, ——, J. M. L. Dahl, L. J. Wicker, and A. J. Clark, 2017: Volatility of Tornadogenesis: An Ensemble of Simulated Nontornadic and Tornadic Supercells in VORTEX2 Environments. *Mon. Weather Rev.*, **145**, 4605–4625, https://doi.org/10.1175/MWR-D-17-0152.1.

Dahl, J. M. L., M. D. Parker, and L. J. Wicker, 2012: Uncertainties in Trajectory Calculations within Near-Surface Mesocyclones of Simulated Supercells, https://doi.org/10.1175/MWR-D-12-00131.1.

——, ——, and ——, 2014: Imported and Storm-Generated Near-Ground Vertical Vorticity in a Simulated Supercell. *J. Atmospheric Sci.*, **71**, 3027–3051, https://doi.org/10.1175/JAS-D-13-0123.1.

Davies-Jones, R., and H. Brooks, 1993: Mesocyclogenesis From a Theoretical Perspective. *The Tornado: Its Structure, Dynamics, Prediction, and Hazards*, C. Church, D. Burgess, C. Doswell, and R. Davies-Jones, Eds., Vol. 79 of, American Geophysical Union, 105–114, https://doi.org/10.1029/GM079p0105.

——, R. J. Trapp, and H. B. Bluestein, 2001: Tornadoes and Tornadic Storms. *Severe Convective Storms*, C.A. Doswell, Ed., American Meteorological Society, 167–221, https://doi.org/10.1007/978-1-935704-06-5_5.

Deardorff, J. W., 1974: Three-dimensional numerical study of turbulence in an entraining mixed layer. *Bound.-Layer Meteorol.*, **7**, 199–226, https://doi.org/10.1007/BF00227913.

Emanuel, K. A., 1994: *Atmospheric convection*. Oxford University Press 580pp.

Finley, C. A., M. Elmore, L. Orf, and B. D. Lee, 2023: Impact of the Streamwise Vorticity Current on Low-Level Mesocyclone Development in a Simulated Supercell. *Geophys. Res. Lett.*, **50**, e2022GL100005, https://doi.org/10.1029/2022GL100005.

Fischer, J., and J. M. L. Dahl, 2020: The Relative Importance of Updraft and Cold Pool Characteristics in Supercell Tornadogenesis Using Highly Idealized Simulations. *J. Atmospheric Sci.*, **77**, 4089–4107, https://doi.org/10.1175/JAS-D-20-0126.1.

——, and ——, 2022: Transition of Near-Ground Vorticity Dynamics during Tornadogenesis. *J. Atmospheric Sci.*, **79**, 467–483, https://doi.org/10.1175/JAS-D-21-0181.1.

Accepted for publication in *Journal of the Atmospheric Sciences*. DOI 10.1175/JAS-D-24-0227.1.

——, ——, B. E. Coffer, J. L. Houser, P. M. Markowski, M. D. Parker, C. C. Weiss, and A. Schueth, 2024: Supercell Tornadogenesis: Recent Progress in Our State of Understanding, https://doi.org/10.1175/BAMS-D-23-0031.1.

French, M. M., H. B. Bluestein, I. PopStefanija, C. A. Baldi, and R. T. Bluth, 2013: Reexamining the Vertical Development of Tornadic Vortex Signatures in Supercells, https://doi.org/10.1175/MWR-D-12-00315.1.

Fujita, T. T., G. S. Forbes, and T. A. Umenhofer, 1976: Close-up View of 20 March 1976 Tornadoes: Sinking Cloud Tops to Suction Vortices. *Weatherwise*, **29**, 116–145, https://doi.org/10.1080/00431672.1976.10544142.

Houser, J. L., H. B. Bluestein, and J. C. Snyder, 2015: Rapid-Scan, Polarimetric, Doppler Radar Observations of Tornadogenesis and Tornado Dissipation in a Tornadic Supercell: The "El Reno, Oklahoma" Storm of 24 May 2011, https://doi.org/10.1175/MWR-D-14-00253.1.

Huang, W., and M. Xue, 2023: Sub-vortices Within a Numerically Simulated Tornado: The Role of Unstable Vortex Rossby Waves. *J. Atmospheric Sci.*, **1**, https://doi.org/10.1175/JAS-D-22-0237.1.

Jiang, Q., and D. T. Dawson, 2023: The Impact of Surface Drag on the Structure and Evolution of Surface Boundaries Associated with Tornadogenesis in Simulated Supercells, https://doi.org/10.1175/MWR-D-23-0050.1.

Lilly, D. K., 1982: The Development and Maintenance of Rotation in Convective Storms. *Intense Atmospheric Vortices. Topics in Atmospheric and Oceanographic Sciences.*, L. Bengtsson and J. Lighthill, Eds., Springer Berlin Heidelberg, 149–160, https://doi.org/10.1007/978-3-642-81866-0_12.

Markowski, P., Y. Richardson, and G. Bryan, 2014: The Origins of Vortex Sheets in a Simulated Supercell Thunderstorm. *Mon. Weather Rev.*, **142**, 3944–3954, https://doi.org/10.1175/MWR-D-14-00162.1.

Markowski, P. M., 2016: An Idealized Numerical Simulation Investigation of the Effects of Surface Drag on the Development of Near-Surface Vertical Vorticity in Supercell Thunderstorms. *J. Atmospheric Sci.*, **73**, 4349–4385, https://doi.org/10.1175/JAS-D-16-0150.1.

Accepted for publication in *Journal of the Atmospheric Sciences*. DOI 10.1175/JAS-D-24-0227.1.

——, and G. H. Bryan, 2016: LES of Laminar Flow in the PBL: A Potential Problem for Convective Storm Simulations, https://doi.org/10.1175/MWR-D-15-0439.1.

Meng, Z., and Coauthors, 2018: The Deadliest Tornado (EF4) in the Past 40 Years in China. *Weather Forecast.*, **33**, 693–713, https://doi.org/10.1175/WAF-D-17-0085.1.

Morrison, H., and W. W. Grabowski, 2008: Modeling Supersaturation and Subgrid-Scale Mixing with Two-Moment Bulk Warm Microphysics. *J. Atmospheric Sci.*, **65**, 792–812, https://doi.org/10.1175/2007JAS2374.1.

Murdzek, S. S., P. M. Markowski, and Y. P. Richardson, 2020: Simultaneous Dual-Doppler and Mobile Mesonet Observations of Streamwise Vorticity Currents in Three Supercells. *Mon. Weather Rev.*, **148**, 4859–4874, https://doi.org/10.1175/MWR-D-20-0239.1.

Oliveira, Xue, Roberts, Wicker, and Yussouf, 2019: Horizontal Vortex Tubes near a Simulated Tornado: Three-Dimensional Structure and Kinematics. *Atmosphere*, **10**, 716, https://doi.org/10.3390/atmos10110716.

Orf, L., R. Wilhelmson, B. Lee, C. Finley, and A. Houston, 2017: Evolution of a Long-Track Violent Tornado within a Simulated Supercell. *Bull. Am. Meteorol. Soc.*, **98**, 45–68, https://doi.org/10.1175/BAMS-D-15-00073.1.

Parker, M. D., and J. M. L. Dahl, 2015: Production of Near-Surface Vertical Vorticity by Idealized Downdrafts. *Mon. Weather Rev.*, **143**, 2795–2816, https://doi.org/10.1175/MWR-D-14-00310.1.

Pleim, J. E., 2006: A Simple, Efficient Solution of Flux–Profile Relationships in the Atmospheric Surface Layer. *J. Appl. Meteorol. Climatol.*, **45**, 341–347, https://doi.org/10.1175/JAM2339.1.

——, 2007: A Combined Local and Nonlocal Closure Model for the Atmospheric Boundary Layer. Part I: Model Description and Testing. *J. Appl. Meteorol. Climatol.*, **46**, 1383–1395, https://doi.org/10.1175/JAM2539.1.

Roberts, B., and M. Xue, 2017: The Role of Surface Drag in Mesocyclone Intensification Leading to Tornadogenesis within an Idealized Supercell Simulation. *J. Atmospheric Sci.*, **74**, 3055–3077, https://doi.org/10.1175/JAS-D-16-0364.1.

Accepted for publication in *Journal of the Atmospheric Sciences*. DOI 10.1175/JAS-D-24-0227.1.

——, ——, A. D. Schenkman, and D. T. Dawson, 2016: The Role of Surface Drag in Tornadogenesis within an Idealized Supercell Simulation. *J. Atmospheric Sci.*, **73**, 3371–3395, https://doi.org/10.1175/JAS-D-15-0332.1.

Rotunno, R., P. M. Markowski, and G. H. Bryan, 2017: "Near Ground" Vertical Vorticity in Supercell Thunderstorm Models. *J. Atmospheric Sci.*, **74**, 1757–1766, https://doi.org/10.1175/JAS-D-16-0288.1.

Schenkman, A. D., M. Xue, and A. Shapiro, 2012: Tornadogenesis in a Simulated Mesovortex within a Mesoscale Convective System. *J. Atmospheric Sci.*, **69**, 3372–3390, https://doi.org/10.1175/JAS-D-12-038.1.

——, ——, and M. Hu, 2014: Tornadogenesis in a High-Resolution Simulation of the 8 May 2003 Oklahoma City Supercell. *J. Atmospheric Sci.*, **71**, 130–154, https://doi.org/10.1175/JAS-D-13-073.1.

——, ——, and D. T. Dawson II, 2016: The Cause of Internal Outflow Surges in a High-Resolution Simulation of the 8 May 2003 Oklahoma City Tornadic Supercell. *J. Atmospheric Sci.*, **73**, 353–370, https://doi.org/10.1175/JAS-D-15-0112.1.

Schueth, A., C. Weiss, and J. M. L. Dahl, 2021: Comparing Observations and Simulations of the Streamwise Vorticity Current and the Forward Flank Convergence Boundary in a Supercell Storm. *Mon. Weather Rev.*, https://doi.org/10.1175/MWR-D-20-0251.1.

Sherburn, K. D., and M. D. Parker, 2019: The Development of Severe Vortices within Simulated High-Shear, Low-CAPE Convection. *Mon. Weather Rev.*, **147**, 2189–2216, https://doi.org/10.1175/MWR-D-18-0246.1.

Smagorinsky, J., 1963: GENERAL CIRCULATION EXPERIMENTS WITH THE PRIMITIVE EQUATIONS: I. THE BASIC EXPERIMENT. *Mon. Weather Rev.*, **91**, 99–164, https://doi.org/10.1175/1520-0493(1963)091<0099:GCEWTP>2.3.CO;2.

Snook, N., M. Xue, and Y. Jung, 2019: Tornado-Resolving Ensemble and Probabilistic Predictions of the 20 May 2013 Newcastle–Moore EF5 Tornado. *Mon. Weather Rev.*, **147**, 1215–1235, https://doi.org/10.1175/MWR-D-18-0236.1.

Accepted for publication in *Journal of the Atmospheric Sciences*. DOI 10.1175/JAS-D-24-0227.1.

Sun, Z., M. Xue, K. Zhu, and B. Zhou, 2019: Prediction of an EF4 supercell tornado in Funing, China: Resolution dependency of simulated tornadoes and their structures. *Atmospheric Res.*, **229**, 175–189, https://doi.org/10.1016/j.atmosres.2019.06.019.

Tao, T., and T. Tamura, 2020: Numerical Study of the 6 May 2012 Tsukuba Supercell Tornado: Vorticity Sources Responsible for Tornadogenesis. *Mon. Weather Rev.*, **148**, 1205–1228, https://doi.org/10.1175/MWR-D-19-0095.1.

Xu, X., M. Xue, and Y. Wang, 2015: The Genesis of Mesovortices within a Real-Data Simulation of a Bow Echo System. *J. Atmospheric Sci.*, **72**, 1963–1986, https://doi.org/10.1175/JAS-D-14-0209.1.

Xue, M., K. Zhao, M. Wang, Z. Li, and Y. Zheng, 2016: Recent significant tornadoes in China. *Adv. Atmospheric Sci.*, **33**, 1209–1217, https://doi.org/10.1007/s00376-016-6005-2.

Yokota, S., H. Niino, H. Seko, M. Kunii, and H. Yamauchi, 2018: Important Factors for Tornadogenesis as Revealed by High-Resolution Ensemble Forecasts of the Tsukuba Supercell Tornado of 6 May 2012 in Japan. *Mon. Weather Rev.*, **146**, 1109–1132, https://doi.org/10.1175/MWR-D-17-0254.1.

Accepted for publication in *Journal of the Atmospheric Sciences*. DOI 10.1175/JAS-D-24-0227.1.